Recent advances in chemical and magnetic imaging of surfaces and interfaces by XPEEM

2008 J. Phys.: Condens. Matter 20 093002

(http://iopscience.iop.org/0953-8984/20/9/093002)

J. Phys.: Condens. Matter **20** (2008) 093002 (22pp) doi:10.1088/0953-8984/20/9/093002

TOPICAL REVIEW

Recent advances in chemical and magnetic imaging of surfaces and interfaces by XPEEM

A Locatelli[1] **and E Bauer**[2]

[1] Sincrotrone Trieste S.C.p.A., S.S. 14, km 163.5 in Area Science Park, 34012 Basovizza, Trieste, Italy
[2] Department of Physics, Arizona State University, Tempe, AZ 85274-1504, USA

E-mail: andrea.locatelli@elettra.trieste.it

Received 4 October 2007, in final form 2 December 2007
Published 15 February 2008
Online at stacks.iop.org/JPhysCM/20/093002

Abstract
Synchrotron-based photoemission electron microscopy (XPEEM) is one of the most powerful spectro-microscopic techniques for the investigation of surfaces, interfaces, thin films and buried layers. By exploiting the tunability and polarizability of x-ray sources as well as progress in electron optics design, modern XPEEM instruments can perform several x-ray spectroscopic investigations with a lateral resolution of a few tens of nanometres. We review here the latest developments in XPEEM, illustrating the state of the art capabilities of the technique. The usefulness of chemical and magnetic imaging XPEEM methods is demonstrated by examples of fundamental and applied studies in surface and material sciences, as well as other fields of application ranging from magnetism to biology and geology.

(Some figures in this article are in colour only in the electronic version)

Contents

1. Introduction

The unique characteristics of x-ray radiation from third-generation synchrotron radiation sources have prompted considerable progress in spectro-microscopy. The high flux and brilliance of synchrotron light along with its tunability and polarizability allows implementation of laterally resolved applications of the most important spectroscopic methods [1]. X-ray photoemission electron microscopy (XPEEM) fully exploits the many advantages of synchrotron radiation: it overcomes the limited elemental sensitivity

of PEEM with conventional UV sources and provides unprecedented opportunities to image surfaces and thin films with chemical [2–5] and magnetic sensitivity [6–8]. The applications of XPEEM are not limited to surface and materials science, but are expanding to novel fields like geology [9], medicine [10] and biology [11].

XPEEM instruments have evolved much in the last decade, reaching a lateral resolution of a few tens of nanometres and full spectroscopic capability [12–15]. Furthermore, the imminent availability of a new generation of instruments implementing aberration correction is pushing the lateral resolution limit well into the nanometre range [16, 17], opening up new exciting developments. XPEEM not only excels in lateral resolution but also in time resolution, as demonstrated by recent experiments on magnetization dynamics with resolution less than 100 ps [18–20].

Driven by the strong interest in surface processes occurring at submicron length scales, the use of PEEM instruments has become widespread. Most third-generation synchrotron radiation facilities now host microscopes served by dedicated beamlines. Following the first applications with synchrotron radiation [21, 22], PEEM experiments made large use of x-ray absorption spectroscopy (XAS) and its related techniques. In combination with linear and circular dichroism (MLD and MCD, respectively) PEEM has become the main tool for imaging the magnetic state of surfaces, thin films and buried interfaces [6–8], which is one of most successful applications of synchrotron-based microscopy. The availability of instruments equipped with an energy filter has also opened the possibility of performing x-ray photoelectron spectroscopy (XPS). This adds lateral sensitivity to electron spectroscopy for chemical analysis (ESCA) and ultra-violet photoelectron spectroscopy (UPS) so that synchrotron radiation PEEM instruments can probe the local chemical state and electronic structure, respectively [23]. Finally, the combination of PEEM with low-energy electron microscopy (LEEM) into a single instrument adds structure sensitivity and diffraction techniques to spectroscopy, enabling an effective multi-technique approach to the study of surfaces [13–15].

In this review we focus on recent progress in synchrotron-based XPEEM research. Instrumental aspects and experimental methodologies including time resolved techniques are briefly discussed in section 2. Sections 3 and 4 describe in detail chemical and magnetic PEEM applications, respectively, and are central to this work. Whenever possible we avoided overlapping with earlier reviews, and concentrated mainly on more recent work done at Elettra. Selected examples were chosen to illustrate the current capabilities of XPEEM and its ability to solve fundamental problems in fields such as surface and material sciences, often emphasizing the power and usefulness of a combined LEEM–PEEM approach.

2. XPEEM instrumentation and methods

2.1. Operating principle

The photoemission electron microscope images a specimen that is illuminated with soft x-rays or ultra-violet (UV) radiation. The emitted electrons are accelerated by a strong field in the objective lens, of which the specimen is an integral part. Therefore the objective lens is also called a 'cathode' lens. The objective produces a magnified image of the specimen, which is further magnified by one or several additional lenses onto a two-dimensional image detector. The detector is usually a multi-channel plate image intensifier—phosphorus screen combination and the image on the screen is recorded with a CCD camera.

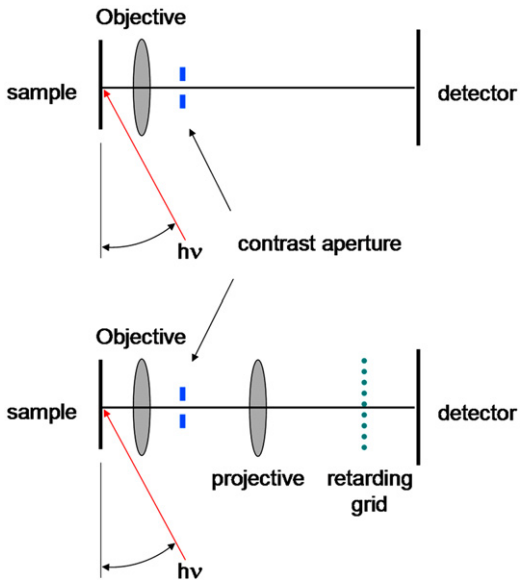

Figure 1. Schematic diagrams of a PEEM in its simplest configuration. For explanation see text (colour online).

2.2. PEEM instruments and operation modes

PEEM instruments can have either purely electrostatic lenses or magnetic lenses. Many of them have no energy filter but systems with an energy filter, either band pass or high pass, are becoming increasingly used. A version that combines PEEM with LEEM and a band pass energy filter, the spectroscopic photoemission and low-energy electron microscope ('SPELEEM'), is used today in many synchrotron radiation sources. This instrument is particularly powerful because of the complementary information obtained with LEEM and LEED. PEEM instruments, in which the chromatic and spherical aberrations of the objective lens are corrected, are still in the commissioning phase (SMART at BESSY2 [16, 24, 25]) or in the development state (PEEM3 at ALS [17, 26, 27]).

Most instruments have been described in original and review papers [12, 15, 28–32] so that we briefly discuss here for completeness only two instruments. The instrument used in the first synchrotron radiation PEEM experiments [21, 22, 28] is shown in figure 1 (top). It consists only of an objective lens, an image detector [22] and an aperture ('contrast aperture') in the back focal plane of the objective lens, which limits the angular acceptance. More recent instruments have one or more lenses after the objective to increase the magnification; correctors for astigmatism and a retarding grid as a high-pass

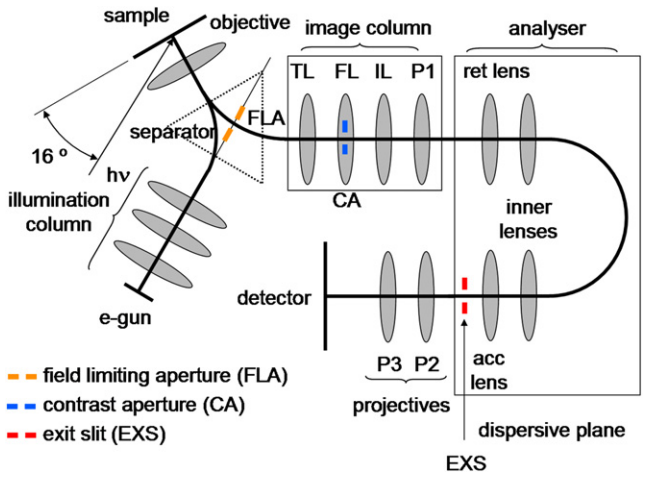

Figure 2. Schematic diagram of the SPELEEM. For explanation see text (colour online).

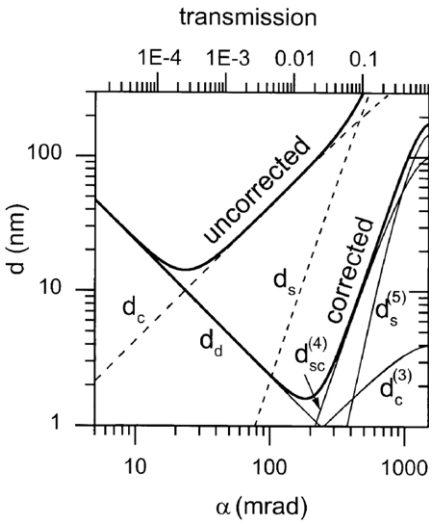

Figure 3. Calculated resolution limit and transmission as a function of the acceptance angle for the SMART microscope. Curves corresponding to corrector on and off are compared and show the significant gain in transmission as well as resolution. The dominant contributions of diffraction (d_d), chromatic (d_c) and spherical (d_s) aberrations are indicated by the labels. Reproduced from [25] with copyright permission from World Scientific.

energy filter (see figure 1 bottom). Instruments combining PEEM with LEEM, such as the SPELEEM [13, 14], have a much more sophisticated optical layout, as illustrated in figure 2.

The SPELEEM allows three basic operation modes:

(i) *Energy filtered imaging.* The sample is illuminated with x-rays to excite photoemission. The lenses labelled FL, IL and P1 magnify the specimen image produced by the objective. A slit is inserted in the dispersive plane of the analyser in order to select the desired energy of the emitted electrons. The specimen image is finally projected onto the detector with the projective lenses P2 and P3. The contrast aperture in the diffraction plane limits the angular acceptance for optimum resolution.

(ii) *Energy filtered micro-diffraction.* IL and P1 image the diffraction pattern produced by the objective rather than the specimen. Insertion of the analyser exit slit allows angle resolved photoemission and x-ray photoelectron diffraction measurements. The probed area is selected by positioning the field-limiting aperture in the image plane after the objective lens.

(iii) *Micro-XPS, or dispersive plane operation.* IL and P1 are as in (i), but the energy slit is not inserted. The two projectors, P2 and P3, are used to image the dispersive plane of the analyser onto the detector. The dispersive plane appears as a line, whose intensity profile represents the photoemission spectrum. In this operation mode the microscope reaches its best energy resolution. The field-limiting and contrast apertures determine the probed area and angular acceptance, respectively.

2.3. Lateral resolution

The lateral resolution of PEEM and LEEM instruments is determined by the chromatic and spherical aberrations of the objective lens. It increases with the angular aperture of the imaging beam linearly and with its third power, respectively. The angular aperture is limited by the contrast aperture, which causes diffraction. The resolution limit can be estimated by minimizing the square root of the sum of the diameters of the confusion disks produced by spherical aberration, chromatic aberration and diffraction at the contrast aperture. Numerous calculations have been made for a wide variety of lens configurations (see for example [33–35]) yielding a limit of about 6 nm for 10 eV electrons and an energy width of 0.5 eV when the optimum aperture is used. While this is, in principle, achievable in LEEM, the usually lower intensity in XPEEM requires a larger contrast aperture which deteriorates the resolution. As a consequence, the best well-documented XPEEM resolutions are in the low 10 nm range, although occasionally resolution values in the nanometre range have been claimed.

In order to achieve a resolution in the nanometre range in XPEEM the optimum aperture has to be increased by correcting spherical and chromatic aberration. In the aberration-corrected instruments SMART and PEEM3 this is done by an electron mirror, combined with a highly symmetric beam separator [16, 17, 24–27]. The elimination of the chromatic and spherical aberration leaves only higher-order aberrations and leads to a much larger optimum angular aperture, resulting in a significant improvement of the transmission and of the resolution. The improvement that can be achieved in this manner depends on the specific design of the electron optics. Crucial factors are the start energy of the electrons and their energy spread. The calculations made for the PEEM3 indicate an optimum resolution of 4 nm at about 1% transmission for secondary electron imaging without an energy filter [17]. Less than 2 nm is expected for the SMART, which uses an energy filter [25]. The resolution and transmission of the uncorrected and corrected microscope are compared in figure 3. The calculations were made for a start energy of 10 eV and an energy spread of 2 eV.

Another ingenious method of aberration correction, which combines a pulsed radiation source, time-dependent lens excitation and delay line detection, has been shown to improve resolution and contrast, though only at low magnifications so far [36, 37]. Aberration correction methods involving numerical steps, such as the moving focus [38] or phase retrieval method, have also been proposed but no success has yet been achieved.

2.4. Comparison with the scanning photoelectron emission microscope

It is useful to compare the PEEM to another widely used experimental method, scanning photoelectron emission microscopy (SPEM). In SPEM the lateral resolution is determined by the lateral dimensions (i.e. the full width half maximum) of the illuminating photon beam, which is usually focused by special diffractive elements obtained by lithographic techniques ('Fresnel lenses' or 'zone plates'). The lateral resolution is limited by the diffraction limit of the zone plate as well as by constraints in the geometry of the collection system and the available photoelectron flux. We underline that the resolution limit for SPEM is at least an order of magnitude larger than for zone plate imaging in full field transmission mode, which has recently demonstrated a record 13 nm [39]. The most advanced instruments, such as the SPEM operating at Elettra, reach a lateral resolution of ∼200 nm [40]. In PEEM the photon illumination does not limit the attainable lateral resolution. The limit is instead set by the aberrations introduced by the electron optics. This gives PEEM a significant advantage over SPEM in terms of lateral resolution (in principle less than 10 nm), which will be further enhanced in aberration correction PEEM instruments.

The spectroscopic ability of SPEM is superior to that of PEEM, because SPEM can exploit the full potential of multi-channel hemispherical energy analysers developed for laterally averaged x-ray photoelectron spectroscopy. The energy resolution performance of SPEM at Elettra is 0.2 eV [41], but can be improved in principle by at least a factor of ten. A similar energy resolution was demonstrated in the SPELEEM at Elettra in dispersive plane operation [15]. In the imaging mode, the energy resolution of the same instrument increases to about 0.3 eV.

It is important to note that the PEEM detection mode is 'parallel'. Photoelectrons emitted from different areas within the microscope field of view are collected simultaneously. On the contrary, SPEM data acquisition is 'sequential'. Each pixel in the SPEM image is obtained after moving the sample with respect to the photon beam, which is thus scanned across the specimen surface. This procedure is less efficient and can cause artefacts when following dynamical processes [42].

2.5. Beamline design

High lateral resolution requires high flux density in the specimen area imaged by the microscope. Owing to the low photoelectron yield in core level photoemission, high flux density is thus demanded from the beamline. This requirement is best met by employing undulator sources together with efficient micro-focusing of the photon beam and medium energy resolution of the monochromator. Such criteria inspired the design of the 'Nanospectroscopy' beamline at Elettra [43] and the SILS beamline at SLS [44], which anticipated similar beamlines at other synchrotron radiation facilities.

Typically, XPEEM beamlines are served by undulators based on the Sasaki design [45], which provides high brilliance and selectable polarization. The availability of two rather than one undulator is particularly useful for magnetic imaging. Switching of the photon helicity is obtained by setting the two undulators to opposite phases, alternatively 'tuning' only one undulator to the monochromator energy while 'detuning' the other one [46]. This method allows inversion of helicity within a few seconds, while minimizing the disturbance to the storage ring orbit.

A crucial aspect in beamline design is the focusing of the photon beam at the microscope. Special adaptable bendable mirrors have been developed for this purpose. Such mirrors are bent by applying unequal moments to their ends, which allow fine control of the focusing of the beam. Profiles approximating ellipses up to the fourth polynomial order can be produced, which allow spot size down to a few micrometres to be obtained [47]. Unfortunately, the mirrors cannot be used to defocus the beam in order to illuminate a wider area on the sample. Under such conditions, the spot is affected by residual aberrations and slope errors, resulting in a strongly inhomogeneous illumination. Variable spot size refocusing optics suitable for XPEEM have been demonstrated recently [48].

The beam spot is typically wider along the horizontal direction, owing to the larger size of the source along the plane of the orbit. In microscopes where the specimen is vertical the grazing incidence of the photons imposed by the objective lens geometry produces an elongated shape of the beam spot. This type of illumination is suitable only when operating the microscope at fields of view less than the vertical size of the beam, typically less than a few microns. Imaging becomes impossible at smaller magnifications, because the beam spot cannot be magnified by the refocusing optics. In order to avoid this severe limitation, the PEEM instrument can be rotated, so that the specimen is slightly tilted with respect to the horizontal plane and a circularly shaped beam spot is produced. This simple solution, now available in commercial PEEM instruments, allows homogeneous and efficient illumination both at small and intermediate fields of view.

2.6. XPEEM spectroscopies

The illumination of the specimen with x-rays excites a broad electron spectrum consisting of the primary unscattered or elastically scattered photoelectrons, inelastically scattered electrons, Auger electrons and secondary electrons. By imaging with these electrons with or without selecting their kinetic energy, the PEEM can perform laterally resolved versions of most widely used x-ray spectroscopy techniques. The available techniques may be divided in two groups. The first group uses electrons whose energy is characteristic for the material studied. This requires an energy filter, preferably a

band pass. The second group makes use of the absorption of photons at energies characteristic of the materials studied. The absorption is measured via the secondary electron emission intensity, which requires no energy filter, although this is useful for enhancing the spatial resolution.

2.6.1. X-ray electron emission spectroscopies.

- *X-ray photoelectron spectroscopy (XPS).* The PEEM detects electrons emitted from atomic core levels with kinetic energy $\mathbf{E}_{\mathrm{kin}} = \mathbf{h}\boldsymbol{\nu} - \mathbf{E}_{\mathrm{bin}} - \boldsymbol{\varphi}$, where $\mathbf{E}_{\mathrm{bin}}$ is the core level binding energy, $\mathbf{h}\boldsymbol{\nu}$ is the photon energy and $\boldsymbol{\varphi}$ the work function. Typically $\mathbf{h}\boldsymbol{\nu}$ is fixed and $\mathbf{E}_{\mathrm{kin}}$ is varied, which allows probing of the chemical state of the emitting atoms by measuring their binding energies. The intensity of the photoemission signal is proportional to the number of emitters in the topmost layers within their energy-dependent escape depth, and thus provides straightforward and quantitative information about the surface chemical composition. Optimal surface sensitivity is achieved by an appropriate choice of the photon energy, so that $\mathbf{E}_{\mathrm{kin}}$ is at the minimum of the inelastic mean free path of the electrons in the matter, generally between 50 and 150 eV. Probing valence band states in this manner makes PEEM particularly sensitive to the surface band structure, including surface states and resonances. Several methods are possible with state-of-the-art instruments: spectral imaging (or XPS imaging), spectroscopy mode (micro-XPS) or diffraction mode (micro-XPD), which allows probing the local order and structure around the emitter.
- *Auger electron spectroscopy.* The energy, intensity and shape of Auger electron spectra contain information on core states and valence band states, although this is difficult to disentangle. With strong and sharp core level spectra available for imaging, Auger electrons have been little used up to now for imaging

2.6.2. X-ray absorption spectroscopy (XAS). The PEEM images the secondary electron emission at fixed kinetic energy as a function of the photon energy $\mathbf{h}\boldsymbol{\nu}$. When $\mathbf{h}\boldsymbol{\nu}$ matches a core level energy, a peak in the secondary emission intensity is observed. Such resonances arise from transitions from core levels into unoccupied valence states via excitation processes occurring during the filling of the core holes. They are characteristic fingerprints of the emitter chemical state, so that PEEM allows chemical maps to be obtained. Furthermore, x-ray absorption near-edge spectroscopy (XANES) provides a wealth of information about the emitter: site location and valence state. Due to the very low energy of the secondary electrons (less than 10 eV), their mean free path is relatively large. XAS and XANES can thus probe buried interfaces or films up to a depth of ∼10 nm. The resolving power of the monochromator determines the attainable energy resolution so that, in principle, no energy filter is required.

X-ray absorption is frequently dichroic, i.e. it depends upon the orientation of the $\mathbf{E}$ vector of the wave with respect to the sample. Examples are oriented molecules when the absorption for $\mathbf{E}$ parallel and $\mathbf{E}$ perpendicular to the molecular axis is different or, more important, in magnetic materials. This makes two special modes of XAS imaging very important.

- *Magnetic circular dichroism.* X-ray magnetic circular dichroism (XMCD) is a well-established technique to probe the magnetic state of ferromagnetic 3d transition metals and their compounds. Excitation of 2p electrons with circularly polarized radiation transfers the photon angular momentum to the spin of the excited photoelectron, which is used to probe the unfilled 3d states in the spin-split valence band. Quantitative sum rules allow spin and orbital magnetic moments to be obtained from XMCD spectra [49–51]. At resonance, the secondary electron yield is proportional to the dot product between the magnetization direction and the photon helicity vector, which is parallel or antiparallel to the beam propagation direction according to the handedness of the circular polarization. Thus, local differences in the orientation of the magnetization produce differences in the XAS intensity, and these allow imaging domains and domain walls in thin magnetic films and surfaces. The XMCD image is obtained by subtraction of two PEEM images obtained with opposite helicity, i.e. $I_{\mathrm{XMCD}} = (I_{\mathrm{minus}} - I_{\mathrm{plus}})/(I_{\mathrm{minus}} + I_{\mathrm{plus}})$. Domains with opposite orientation along the photon beam direction appear as bright and dark regions; domains aligned normal to the beam appear in neutral greyscale.
- *Magnetic linear dichroism.* X-ray magnetic linear dichroism (XMLD) PEEM is used in the characterization of antiferromagnetic materials, and is sensitive to the alignment of the magnetic axis $\mathbf{A}$. In XMLD the secondary electron intensity depends upon the charge distribution and magnetism. The magnetic contrast is proportional to $3\cos^2(\theta) - 1$, where θ is the angle between $\mathbf{A}$ and the electric field vector $\mathbf{E}$ [6–8, 52]. XMLD-PEEM can thus image the AFM order, e.g. the alignment of the axis A and the domains. Data are acquired using horizontal and vertical linear polarization of the photons. The XMLD images are usually obtained by subtraction of PEEM images obtained at two energies around the resonances, in order to maximize MLD contrast.

2.7. Time resolved techniques

Time resolved (TR) PEEM brings the time resolution of standard PEEM (a few tens of milliseconds at most) down to the picosecond regime. It is often used in combination with XMCD to investigate the dynamics of surface magnetism. Details of the technique and examples of applications are described extensively in [20, 53, 54], so here we will limit ourselves to a brief description of the method. A TR experiment is performed using a *conventional* PEEM microscope, with or without an energy filter, and stroboscopic illumination. The pulsed nature and well-defined time structure of the x-rays produced in storage rings have been exploited to obtain snapshots of the time evolution of the system under study.

The so-called 'pump and probe' experiments are performed as illustrated in the diagram of figure 4. Firstly the

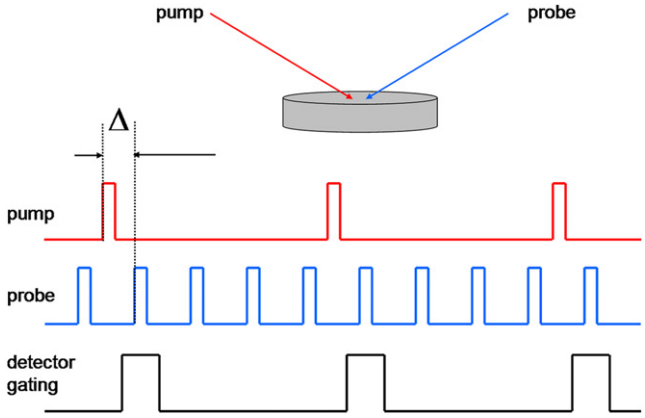

Figure 4. Schematic diagram of a pump–probe experiment. Only the signal starting the pump pulse, which is usually much wider (typically 1–5 ns) than the probe pulse (2–100 ps) is shown. See text for explanation (colour online).

'pump' pulse (e.g. a magnetic or electric field pulse) drives the system into an excited state. Then the 'probe' photons are used to obtain a PEEM image of the system. 'Pump' and 'probe' are synchronized, the latter following the first at a given adjustable delay time Δ. During a single 'probe' pulse only a small number of electrons are emitted. Therefore TR imaging is limited to imaging with secondary electrons and the experiment has to be repeated many times keeping the time delay Δ fixed, until satisfactory statistics is obtained. Typically, hundreds of millions of 'pump'–'probe' cycles are needed. By varying the time interval between 'pump' and 'probe', one can investigate the dynamics of the various stages of the excitation/de-excitation processes. Whenever the repetition rate of the 'pump' pulse is limited, gating of the detector might be required to suppress unwanted x-ray 'probe' pulses.

In magnetization dynamics experiments, a fast rise current pulse flowing into a conductive coplanar waveguide or micro-coil produces the magnetic field pulse excitation. Such structures are lithographically patterned on an insulating substrate. The current pulse is typically generated by a photoconductive switch located in the proximity of the sample. Alternatively, the current pulse can be directly provided by a pulse generator. Details of related methods can be found in [53–55].

The time resolution of the stroboscopic PEEM experiment is primarily determined by the 'probe' pulse width and the jitter in the synchronization, generation and manipulation of the 'pump' and 'probe' signals. Typically, third-generation synchrotron light sources offer dedicated operation modes for TR experiments, with pulse widths ranging from ∼100 ps to the record of 1.6 ps obtained at BESSY2, operating in the so-called 'low-α' mode. The best reported time resolution in TR-XPEEM is in the range 10–70 ps, depending on the operating conditions of the ring [20]. In the future, the availability of free electron laser (FEL) sources will produce tunable x-rays with pulse duration down to the femtosecond range. It has to be kept in mind, however, that femtosecond pulses require much higher flux densities for acceptable image acquisition times. These cause space-charge, local heating and damage problems, which may limit their applicability.

The use a (x, y, t) delayline detector permits a slightly different version of the stroboscopic experiment described above [56]. In this case the PEEM is used as a time-of-flight detector that can reveal single photoemission events with lateral resolution. Depending on the delay from the time-zero (defined by the 'pump' event), each detected 'count' is accumulated into an image corresponding to a certain time interval (or slice). Besides being a means for optimizing collection efficiency, the use of the time-of-flight (TOF) detection method allows obtaining *simultaneously* the complete dynamic evolution of the system.

3. Chemical imaging

Most of the early applications of energy filtered PEEM were limited to metal and semiconductor interfaces. These have already been reviewed [1–4], so that we concentrate here only on the most recent developments. PEEM applications are also extending to fields such as nano-biology, medicine and geology, but their detailed description goes beyond the scope of this paper. The main focus of the section is to illustrate the potential of energy filtered PEEM, combined with low-energy electron microscopy (LEEM) and related methods such as darkfield imaging and micro-LEED. We will emphasize the great strength of LEEM–PEEM instruments, where the availability of chemical and structure sensitive techniques in a single instrument enables a real multi-technique approach to the study of processes occurring at surfaces and interfaces. The following sections will present a variety of XPEEM–LEEM examples. The reported work is heterogeneous in nature and has been classified according to the different application fields.

3.1. Thin films and interfaces

3.1.1. Electronic structure and reactivity of thin Mg films. The observed size-dependent chemical activity of metal clusters and thin films has been a long-standing topic in surface science and catalysis, stimulating vast research on the reactivity of low-dimensional systems. An XPEEM study of the oxidation of Mg thin films on W(110) [23] addressed the relationship between dimensionality and reactivity, focusing on the role of quantum electron confinement and its effect on the electronic structure of thin films with different thickness.

As a preliminary, Mg/W(110), a model system for quantum electron confinement [57], was studied with LEEM and XPEEM. The morphology and structure of the film were elucidated in detail, and several phase transitions below and around 1 ML coverage were identified [58]. Using LEEM it was possible to optimize growth conditions to obtain regions of different thicknesses. After exposure to molecular oxygen, the dependence of the oxidation rate on film thickness was quantitatively determined by measuring the intensity of the oxide and metallic Mg 2p components. Figure 5 shows LEEM and XPEEM images of the film after oxidation. The LEEM image shows the thickness-dependent quantum size contrast in electron reflectivity. The XPEEM image represents the

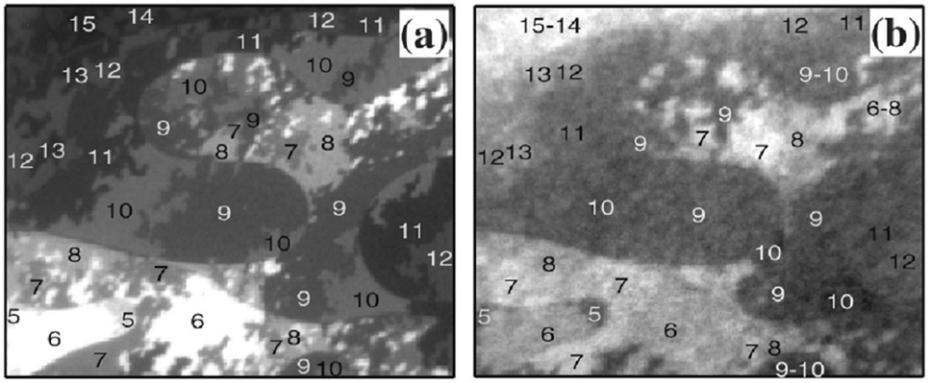

Figure 5. (a) LEEM image of a Mg film in an advanced growth stage. The numbers indicate the film thickness, determined following the reflectivity changes during the film growth. (b) Mg 2p oxide component XPEEM image of the same Mg film, after exposure to 9 Langmuirs of molecular oxygen. The intensity is proportional to the extent of local Mg oxidation. Adapted from [23] with permission. Copyright 2004 by the American Physical Society.

intensity of the Mg 2p oxide component in the same area. The detailed analysis of the two images reveals a complex dependence of the oxidation rate on thickness, with maxima in the range 6–8 and 13–15 layers. Complementary UV-PEEM measurements indicate that the dependence of reactivity upon film thickness is directly correlated to periodic variations in the density of states at the Fermi level, DOS (E_F), induced by quantum well states crossing the Fermi surface. The result of several oxidation experiments is shown in figure 6. As can be seen clearly, there is an almost linear correlation between the measured DOS(E_F) and the reactivity.

These experiments stimulated vivid theoretical interest. Different models were proposed to explain the experimental results, but no consensus has been found yet. According to one model, the observed reactivity modulations originate from a non-adiabatic charge transfer taking place during O_2 dissociation, and result from the linear dependence of the charge transfer rate upon the local DOS (E_F) [59]. A different interpretation attributes the reactivity modulations to the decay length λ above the surface of the electronic local density of states around the Fermi energy [60]. The *ab initio* calculations on the unrelaxed Mg system reveal that λ exhibits an oscillatory behaviour as a function of film thickness, with local maxima corresponding to the highest occupied quantum well state being closest to the Fermi energy, in accord with results from earlier calculations [61].

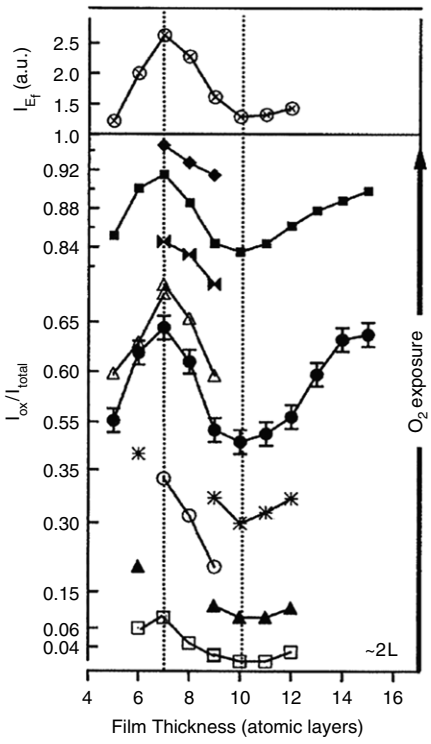

Figure 6. Top: photoemission intensity at the Fermi level measured for areas with different thickness before exposing the film to oxygen. Bottom: plots of the relative weight of the Mg 2p oxide component in different experiments corresponding to different O_2 exposure. Reprinted from [23] with permission. Copyright 2004 by the American Physical Society.

3.1.2. Growth processes on semiconductor substrates: Ge on Si. The strong interest in optoelectronics applications based on nanodevices has motivated numerous microscopy studies of the growth of Ge on Si, concentrating on quantum dots (QD) and their properties. Central issues concern the ability to control positioning and alignment of QDs through self-assembly and understanding of Si–Ge intermixing during island formation.

Experiments on Si(111) demonstrated the usefulness of a combined LEEM–XPEEM approach [62, 63]. In these experiments, LEEM was employed to follow the growth dynamics, and thus to determine QD morphology and structure, and XPEEM to characterize the surface stoichiometry post-growth. Surface composition maps of the islands were obtained from Si 2p and Ge 3d spectra. They show an apparent correlation between the island basal area and the Si concentration in the topmost layers [64]. It turned out that the larger islands have a higher Si concentration, which increases from less than 10% for pyramids up to 25–40% in atoll-like islands. The Si concentration increases with increasing growth temperature, suggesting that Ge–Si alloying is regulated by

kinetic factors. The Si incorporation in the islands might be explained by invoking surface mobility or exchange with the bulk. Yet on the basis of present data it is not possible to identify the dominating diffusion channel.

The influence of a surfactant, Ga, on the growth of Ge on Si(111) was also studied [65]. As shown by combined LEEM and XPEEM measurements, sub-ML adsorption of Ga at 670 K affects the subsequent growth of Ge and induces alignment of the Ge islands. Ge islands nucleate preferentially on the Ga ($\sqrt{3} \times \sqrt{3}$)-R30° phase and at domain boundaries with the (7 × 7) substrate. XPEEM images also indicate a strong correlation between Ga and Ge 3d signals, suggesting segregation of Ga on the island surface during Ge growth.

Another interesting application example was provided by Ge island self-organization occurring on a Si(001) surface decorated with a square pattern of Au dots [66]. Recent XPEEM experiments elucidated the origin of this phenomenon [67]. Upon exposure to air, gold catalyses the oxidation of Si in a circular corona around the pattern, which blocks the diffusion of Au during the following sample preparation (annealing to 550 °C). Subsequent Ge deposition at 450 °C results in the formation of Ge-denuded zones in the oxide regions. The accumulation of Ge outside the Si oxide leads to islanding below the wetting layer critical thickness observed in the metal-free regions of the sample. As shown by XPEEM concentration maps, the deposition of Ge also produces a dramatic transformation in the local concentration of Au. Gold diffuses away from the sites where it was deposited, where only small traces remain, which was attributed to the formation of a Au–Ge eutectic.

3.1.3. Oxide surfaces and interfaces. Oxide surfaces frequently impose severe problems on spectroscopic and microscopic investigations with x-rays, which often produce artefacts in the images or in the spectra. The effect of surface charging and radiation-induced damage was first observed in scanning photoemission microscopy [42]. A similar behaviour is also expected for XPEEM, although the photon flux density illuminating the microscope field of view is lower than in SPEM. Surface charging can be eliminated or at least reduced by simply increasing the sample temperature. Oxygen loss is determined by the radiation dose which is necessary for image acquisition, but can be reduced by minimizing the desorption cross section by appropriate choice of the photon energy. In addition, flux density can have a major influence on the damage created by radiation. The authors observed more or less strong surface reduction under irradiation with a micro-focused soft x-ray beam on $SrTiO_2$, ZrO_2, CeO_2, and TiO_2 [68, 69]. Experiments on oxide nanostructures obtained by local anodic oxidation (LAO) on GaAs and GaAs/AlAs/GaAs demonstrated that prolonged irradiation with soft x-rays (130 eV) can remove several layers of material, and eventually lead to the desorption of the whole LAO oxide [70–74].

Metal nanoparticles on oxide substrates are a challenging research subject for XPEEM. Metal-on-oxide systems show unique characteristics, which determine their chemical activity and selectivity. The typical size of such structures is less than 10 nm, so that only PEEM instruments with aberration correction reach the lateral resolution that is necessary for performing experiments. One-dimensional (1D) metals grown on oxides provide another excellent scientific case for XPEEM. Besides the fundamental interest, the ability to grow in 1D might also open new pathways to the creation of devices based on purely quantum behaviour. The study of their growth and electronic structure is within reach of LEEM–XPEEM, and provides an attractive alternative to the perspective given by STM measurements.

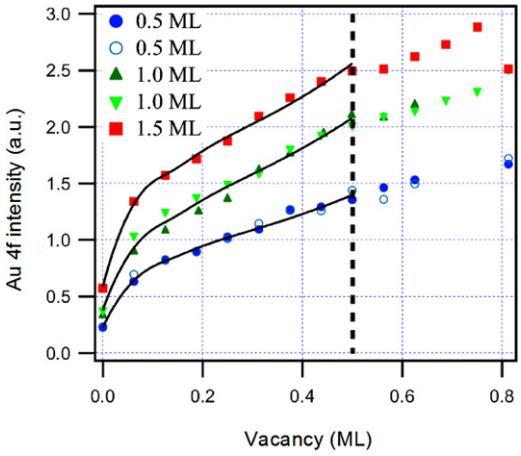

Figure 7. Intensity of the Au 4f emission on the TiO_2 surface as a function of the vacancy concentration for experiments with different Au coverage. The dotted line marks the best (1 × 2) structure; the continuous lines are a fit modelling the transition from cluster to one-dimensional growth (colour online). Reproduced from [69] with copyright permission by the American Physical Society.

In a recent study we proposed a novel pathway to create one-dimensional Au on rutile TiO_2 surfaces, by exploiting surface reduction resulting from irradiation damage [68, 69]. Such Au 'wires' grow during deposition of Au on the oxygen vacancy rows of the (1 × 2) reduced phase formed by electron or photon stimulated desorption of oxygen at intermediate temperatures, ∼ 750 K. Under these conditions, the surface-to-bulk mass transport of O is still inefficient, so that vacancies cannot be filled but reorganize to minimize the repulsive interactions. The observed (1 × 2) LEED was attributed to a metastable (1 × 2) missing-row structure, distinctly different from the (1 × 2) added row which is formed at high temperatures and generally accepted as the stable form of the (1 × 2) reconstruction. This low-temperature (1 × 2) structure has 0.5 ML vacancies. The large interchain distance makes it ideal for studies of one-dimensional phenomena.

Whereas the interaction of Au with the stoichiometric surface is weak, the ordered vacancy template of the (1 × 2) structure provides an abundance of energetically favourable adsorption sites, favouring one-dimensional or two-dimensional growth modes over formation of clusters. The evidence for this change in Au growth mode comes from micro-LEED and XPEEM measurements. Results of experiments of irradiation with 60 eV electrons [69] are illustrated in figure 7, which shows the evolution of the Au 4f intensity as a function of oxygen vacancy density for Au coverage of 0.5, 1.0 and 1.5 ML. Opposed to the small Au

signal observed in the unirradiated areas, there is a strong increase in Au 4f intensity following the development of the (1 × 2) structure. Owing to the short inelastic mean free path of Au 4f photoelectrons with 90 eV kinetic energy, surface and bulk sensitivity are at maximum and minimum, respectively. Therefore, the Au 4f data indicate a transition from cluster growth on the stoichiometric surface to one- or two-dimensional growth on the irradiated surface, resulting from Au adatoms occupying oxygen vacancies. The slower increase of the Au signal after 0.5 ML vacancies was attributed to an electrochemical potential gradient from the surrounding unirradiated regions. We note that Au deposition does not cause an intensity decrease of the superstructure spots in LEED, but rather an increase, which indicates that Au adsorbs on the vacancies with the periodicity of the (1 × 2) template and supports one-dimensional growth. These measurements were complemented by detailed *ab initio* calculations, which indicate strong bonding of Au on TiO_2 bridging vacancies and formation of various types of Au chains (monomers, dimers and trimers) with chain distance dictated by the substrate periodicity.

3.2. Nonlinear processes during surface catalytic reactions

By imaging spatial variations of the surface work function with low-energy photons from deuterium or mercury lamps, conventional UV threshold PEEM has found extensive use in studying spatio-temporal oscillations that develop during simple catalytic surface reactions [75]. The applicability of this method is, however, limited to the observation of space and time characteristics of reaction wavefronts in a restricted number of simple reaction systems, where the chemical composition of the different surface phases is straightforward or can be determined using complementary techniques. There are, however, non-trivial reaction systems were true chemical sensitivity is mandatory. Examples can be found in complex multi-component reaction systems, such as the $NO + H_2$ and $O_2 + H_2$ reactions on Rh(110), which have been successfully studied using SPEM [76]. The SPEM study of sub-ML K/Rh(110) and others systems [77] revealed for the first time reactive phase separation of metal adatoms used as promoters, and stimulated subsequent SPELEEM investigations on reaction-induced reorganization of sub-ML noble metals on Rh(110) [78–82].

The water formation reaction on Rh(110) modified with sub-ML Au has been chosen as a model system for reorganization within adlayers of spectator adspecies. These adsorbates do not actively participate in the reaction but block surface active sites with the macroscopic effect of decreasing the reaction rate. Similarly, Au does not alter the water formation reaction mechanism, so that the Au modified surface still exhibits bistability upon oxidation/reduction [78]. Transitions between O-covered and reduced surface are induced by propagation of elliptical reaction wavefronts.

One of the main results of SPELEEM experiments is that the wavefronts lead to a profound compositional and structural lateral reorganization of the interface [78, 79]. LEEM and micro-LEED were used to monitor the dynamics of front

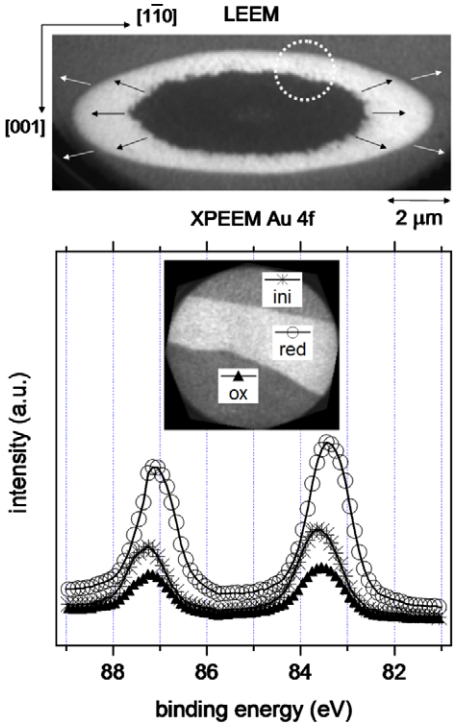

Figure 8. Top: LEEM image (7.7 eV) illustrating the propagation of reduction/oxidation wavefronts on O-covered Rh(110) modified with 0.5 ML Au. The propagation direction is indicated by the arrows; the dotted circle indicates the area probed by XPEEM and shown below. Bottom: Au $4f_{7/2}$ image and spectra taken during front propagation. The spectra are measured on the initial ('ini'), reduced ('red'), and re-oxidized ('ox') surface. Adapted from [78]. Copyright 2004 with permission from Elsevier.

propagation. Figure 8 (top) shows a LEEM image of a reduction front (bright), followed by a concentric oxidation front (dark) moving in the same direction, as indicated by the arrows. Au compositional maps and spectra of the fronts were obtained using XPEEM, by measuring Au 4f core level emission. The spectra in figure 8 (bottom) show clearly that the oxidation front compresses Au into the reduced area, where a saturation layer is formed. On the other hand, the re-oxidized areas are depleted of Au. The simultaneous propagation of the reduction/oxidation fronts thus determines an efficient mass transport of Au across the surface. In the stationary state this leads to the formation of large Au islands and phase separation between Au and O.

The Au–O phase separation is preserved under oxidation conditions. Re-establishing reduction conditions above 550 K readily reacts off the adsorbed oxygen, which in turn allows a quick homogenization of the Au adlayer. This is illustrated by the Au 4f images in figure 9, with a time resolution of 10 s. The Au pattern is preserved under oxidation, but dissolves quickly after reduction conditions are imposed, as evidenced by the equalization of the Au 4f intensity in regions (a) and (b). As demonstrated by LEEM movies, the reduction starts from the O-covered Rh areas, which have higher reactivity than the Au saturated regions. We underline the ability of both XPEEM and LEEM to monitor dynamical processes. Whereas the time resolution of PEEM using core level photoelectrons is

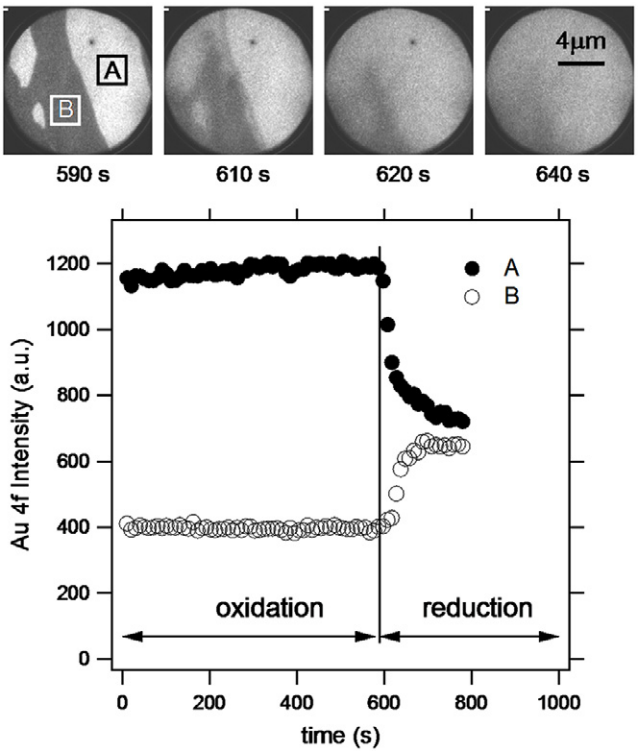

Figure 9. Top: Au 4f images illustrating how Au–O, preserved in oxygen ambient, is dissolved under reduction conditions. Bottom: Au $4f_{7/2}$ average intensity in the areas labelled (a) and (b) (see top), as a function of time. As can be seen, the Au $4f_{7/2}$ intensity measured in (a) and (b) equalizes quickly after imposing reduction. Adapted from [78]. Copyright 2004 with permission from Elsevier.

limited to few seconds per frame, LEEM can image at video rates. LEEM is therefore crucial in following directly dynamic phenomena, such as adatom diffusion and propagation of chemical waves.

The Au–O phase separation described previously is driven by pure energetic principles [79]. As demonstrated by *ab initio* calculations, the mixed Au–O state has a higher total energy than the separated Au and O adsorption states, due to mutual destabilization of Rh–Au and Rh–O bonds in the coadsorbed phase. In static conditions the reduced mobility of adsorbates inhibits phase separation. By creating empty sites on the surface, the reaction enables conditions for the lateral reorganization of the adsorbates, so that phase separation can take place on larger length scales. In practice, pattern formation results from the combined effect of the reaction, adspecies diffusion and interplay of attractive and repulsive interactions between the adsorbates or between the adsorbates and substrate. This is a strongly nonlinear process, which can be modelled by introducing appropriate kinetic equations. Such simple theoretical models predict that adsorbates on catalytic surfaces can form stationary or travelling periodic non-equilibrium nanostructures with well-defined morphology [77, 83, 84].

Theory also predicts that the reaction rate can be used to control the adlayer microstructure wavelength, and through this the catalyst activity [85]. This has prompted new pathways to the creation of surface-supported functional materials with

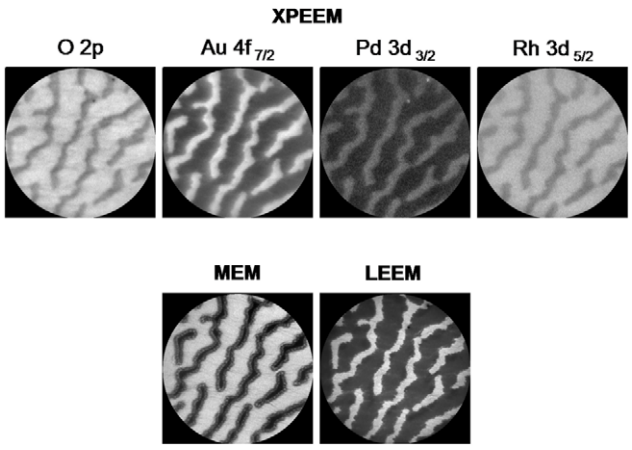

Figure 10. Top: XPEEM images illustrating the formation of Au + Pd stationary patterns, with phase separation of Au and Pd from O. Bottom: LEEM and MEM images for comparison. Adapted with permission from [80]. Copyright 2006 American Chemical Society.

adaptable morphology and reactivity. For the case of Au and Au + Pd adlayers on Rh(110) the water formation reaction has provided a neat experimental demonstration of these predictions [80, 81]. In a narrow temperature range around 800 K, and metal adlayer coverage of 0.45–0.75 ML, regular lamellar structures spontaneously develop at transition from the 'reduced' state (here metal adsorbates are homogeneously distributed on the surface) to the 'oxidized' state. The Au $4f_{7/2}$, Pd $3d_{3/2}$ and O 2p XPEEM images in figure 10 illustrate the phase separation induced by the reaction. The lamellae consist of alternating Au + Pd and O islands. Missing-row reconstruction of the substrate in the O-phase striped areas was nicely demonstrated by darkfield LEEM. In fair agreement with theory [85], the wavelength of periodic structures is found to obey an inverse power-law dependence on the reaction rate, as demonstrated by LEEM experiments in a range of more than two decades variation of pressure of the reactants.

3.3. Material science and nanostructure characterization

Besides the natural application field of XPEEM with chemical sensitivity in surface science, this technique is finding its way in other fields such as materials science and nanostructure characterization. XPEEM is typically employed to get concentration maps at the highest lateral resolution. When sensitivity to the topmost surface layers is crucial, local XPS methods are preferred. This approach has been used to characterize the chemical state of Fe nanoparticles synthesized from Fe_2O_3 through a bonding partner reduction reaction involving the substrate atoms [86]. The study of surface composition gradients in InAs/GaAs QDs (with an average base length of ∼85 nm) is representative of the present capabilities of laterally resolved XPS using PEEM [87]. The concentration of In outside and across the quantum dots was quantitatively obtained by means of high lateral resolution core level spectra. The experimental results point towards strong In surface segregation.

When knowledge of the thin film chemistry is required, XANES is the most appropriate technique. The phase segregation of immiscible mixtures of polystyrene/polymethylmethacrylate (PS/PMMA) was thoroughly studied by XPEEM based on a NEXAFS contrast method and STXM (scanning transmission x-ray microscopy) [88]. More recently, the investigations were extended to the adsorption of fibrinogens (blood proteins) on the same surface [89]. Details of the experimental and instrumental aspects of such investigations have been recently reported in [90].

XANES–XPEEM was also used for the chemical characterization of molecular patterns produced by electron irradiation of aliphatic and aromatic thiol self-assembled monolayers, providing specific information on pristine and irradiated areas at lateral resolution better than 150 nm [91]. More recently, it has been demonstrated that the same approach can be fruitfully employed to obtain spectra from individual oxide nanowires (NW) used as chemiresistors in prototype nanodevices [92]. In this experiment, the NWs are suspended on an insulating support, a non-conducting micro-machined glass metallized on top by deposition of Ti and Au. The special support design allowed minimization of charging artefacts and background emission from the area below the NW. An earlier study of single-walled carbon nanotubes demonstrates the ability of XPEEM to extract quantitative information about their work function distribution [93]. Spectral imaging with C 1s photoelectrons has also been successfully performed [94]. Due to the very low signal levels, minimization of background emission from the Si substrate was mandatory. Growing the nanotubes between 'tall' patterned rods of Si and aligning them perpendicular to the direction of the light obtained efficient illumination shadowing.

3.4. Other applications: mineralogy, biology and medicine

XANES-PEEM with secondary electrons provides a powerful analytical tool for biological samples. The use of UV-PEEM in biology dates back to the 1970s and early applications are reviewed in [95]. In recent years, specific methodologies to look at biological samples have been developed, demonstrating that XANES-PEEM can be employed in the study of complex inorganic structures in biosystems at a high lateral resolution [9, 31]. The usefulness of these approach is illustrated by an increasing number of applications [10, 11, 96, 97], and is representative of the ability of XANES-PEEM to obtain spectroscopic information from small areas.

A remarkable example of the application of XANES-PEEM in the study of biominerals (reviewed in [98]) is provided in [11]. Here, XANES-PEEM unveils the peculiar elemental structure of mineralized and non-mineralized fibrils and filaments produced by microbial cells. Features in local XANES spectra were used to identify the composition and crystalline order of the fibrils (see figure 11). The spectra indicate that only fibrils containing polymer strands (polysaccharides) can template akaganeite pseudo-single crystals with aspect ratios of 1000:1. It has been hypothesized that the cell expels polysaccharide strands to induce FeOOH precipitation in proximity to the cell membrane, which reacts with water and lowers the pH favouring metabolic energy generation.

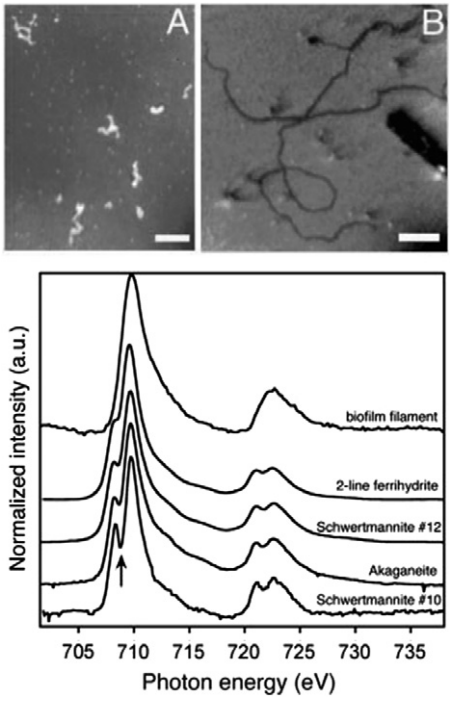

Figure 11. Top: XPEEM images of (A) non-mineralized fibrils from the cloudy water above the biofilm (scale bar, 5 μm) and (B) mineralized filaments and a sheath from the biofilm (scale bar, 1 μm). Bottom: XPEEM Fe L-edge XANES spectra of the FeOOH mineralized looped filament shown in (B), compared with iron oxyhydroxide standards, arranged (bottom to top) in order of decreasing crystallinity, as measured by x-ray diffraction peak broadening. Adapted from [11] with permission from AAAS.

Recently, XPEEM and XANES were used to study the microscopic structure of another important biomineral, red abalone nacre, commonly known as mother of pearl. The exploitation of linear dichroism on the C and O K-edges allowed identification of the orientation of the building blocks of bulk nacre, consisting of alternating layers of an organic matrix and aragonite (with thickness 30 nm and 400–500 nm, respectively). The XANES-PEEM images reveal disorder in the *c*-axis crystallographic orientation of different aragonite tablets, which are not aligned parallel to the growth direction. Adjacent tablets often show a similar orientation, forming columns of irregularly stacked aragonite bricks. By comparing the experimental results with model simulations, it was possible to elucidate the origin of nacre. The organic matrix layer is formed first, with randomly distributed nucleation sites that have no associated crystallographic orientation, while nucleation and growth of aragonite comes in the second stage [97]. The stacked structure of nacre also reveals the origin of its great strength, which is 3000 times stronger than brittle aragonite of which it is composed.

A remarkable application in medical sciences is the study of Gd delivery to glioblastoma cells, aimed at optimizing synchrotron stereotactic radiotherapy. As unambiguously demonstrated by XANES-PEEM, Gd accumulates only at

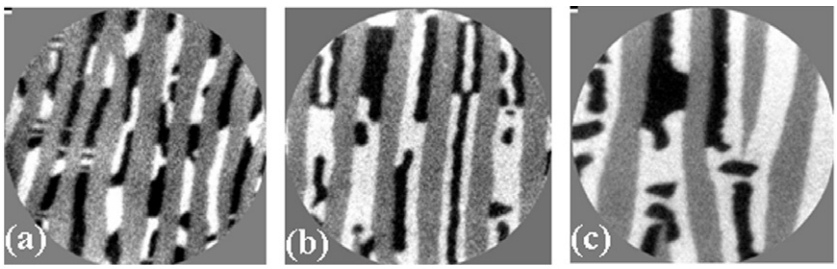

Figure 12. XMCD-PEEM images of MnAs layers on GaAs(100) at room temperature: (a) 120 nm, (b) 215 nm, (c) 300 nm thick. Field of view 5 μm. Reproduced from [111]. Copyright 2006 with permission from Elsevier.

the cancer cell nuclei [99]. Irradiation with 51 kV x-rays stimulates Auger electron emission from Gd, which cleaves DNA double-strands in the cancer cell, inducing their death while preserving healthy cells [10].

All applications described above present numerous and non-trivial experimental difficulties. Radiation damage in organic materials as well as limited UHV compatibility might impede the measurements. Furthermore, the lateral resolution of PEEM can be degraded by field-induced distortions in the proximity of very sharp features on the samples. Local charging on insulating materials can negatively influence both spectroscopy and imaging [100]. Differential thickness coating methods can be effectively employed to minimize such effects (see reference 11 in [31]).

XPEEM has also been employed in geology and mineralogy [9, 101]. For instance, the area selectivity offered by PEEM allows understanding of proportions and space distribution of the different crystal chemistries in the material. Implementing XAS, this technique allows accessing ligand type and bonding character, as well as the oxidation state. Imaging of inclusions and intergrowths in various minerals was recently demonstrated [31, 101].

3.5. UV-FEL-PEEM

The availability of new light sources such as tunable FELs is opening new possibilities using variable wavelength threshold PEEM [102]. Instrumentation, methods and applications in photobiology and material sciences are reviewed in [103].

Owing to the large flux provided by UV-FEL sources, it has been possible to study in real time dynamical processes such as coarsening of $TiSi_2$ islands on Si(111) [104] and formation and migration dynamics of Pt–Si liquid micro-droplets on Si(001) [105]. In these experiments, however, the pulsed nature of the source was not exploited. We remark that UV-FEL-PEEM does not provide true chemical sensitivity, because it is based on work function contrast at threshold emission.

Using tunable UV-FEL in combination with PEEM, threshold potentials for photoionization of various types of melanins were obtained [106]. As indicated by the specific behaviour under UV irradiation, pheomelanin has a lower ionization potential that eumelanin. Thus, pheomelanin decomposes more rapidly in the presence of oxygen, which may explain the greater incidence of skin cancer in red-haired individuals where this pigment is more abundant [107].

4. Magnetic imaging

As already mentioned in section 2, one of the most important applications of XPEEM is magnetic imaging, which makes use of x-ray magnetic circular dichroism for ferromagnetic materials and magnetic linear dichroism for antiferromagnetic materials. The physical foundations of these techniques are described in detail in a recent excellent book on magnetism [8] and their applications up to about 2004 in a review [7]. Therefore, only work done in more recent years or not mentioned in [7, 8] will be discussed here. Most of the work was driven by the desire for higher speed and bit density in the computer and data storage industry. However, some fundamental materials problems were also addressed. The field may be divided in magnetostatic and magnetodynamic studies and we will begin with the first group.

4.1. Fundamental materials problems

MnAs, which long has been known to be ferromagnetic at room temperature and to transform abruptly into a paramagnetic state at 318 K, has attracted much attention in the last 10 years because it can be grown epitaxially on GaAs and has interesting magnetic properties. During cooling from the high-temperature orthorhombic paramagnetic β-phase to the hexagonal ferromagnetic α-phase the crystal lattice expands considerably in the orthorhombic a–b plane/hexagonal basal plane without significant change in the c-direction. In epitaxial layers on GaAs(100), in which the a–b plane/hexagonal plane is perpendicular to the surface, the expansion of this plane during cooling causes a large strain in the layer. This leads to coexistence of the two phases over a temperature range of about 40 K, in which they form stripes along the c-direction whose relative width varies with temperature. This transition was studied extensively as a function of thickness with many methods, in particular with XMCD-PEEM, LEEM and LEED [108–112].

The XMCD-PEEM images in figure 12 give an impression of the ferromagnetic/paramagnetic stripe pattern at room temperature. The black and white regions identify magnetic domains in the α-phase, the vertical grey stripes correspond to the β-phase. The stripe periodicity decreases linearly with increasing thickness. Simultaneously the complexity of the domain structure in the ferromagnetic stripes increases. The magnetization is perpendicular to the stripe direction, pointing in opposite directions in black and white regions. Only at

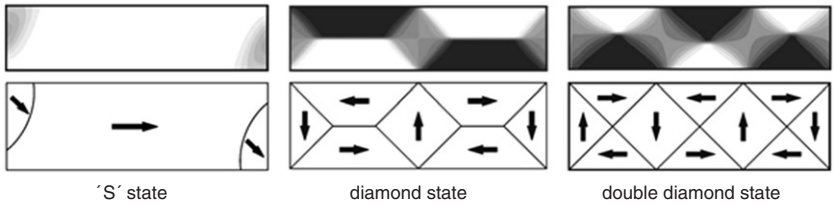

Figure 13. Ferromagnetic domain structures of the films shown in figure 12 according to micromagnetic simulations with schematic magnetization distributions. The images are cross sections through the ferromagnetic stripes, perpendicular to the stripe direction. Reproduced from [111]. Copyright 2006 with permission from Elsevier.

very low MnAs layer thickness, e.g. 40 nm, are the stripes monodomains. The thickness dependence of the domain structure can be explained by the competition between stray field energy E_s and exchange energy E_{ex}: with increasing thickness E_s increases so that the total magnetic energy decreases if domain walls are introduced. This reduces E_s, while increasing E_{ex}, as indicated in the cross sections of the stripes shown in figure 13 [111]. Because of the small escape depth of the secondary electrons used in XMCD-PEEM only the magnetization in the near-surface region of the film is seen in the images.

When a layer is heated from the ferromagnetic single domain state at low temperatures then strongly elongated islands of the β-phase form initially, which grow in length to form continuous stripes. They grow in width with further temperature increase. When these stripes reach a critical, thickness-dependent width, magnetic domains with the opposite magnetization direction form in the ferromagnetic monodomain stripes between the β-stripes, rearrange continuously with increasing temperature to form the configurations seen in figure 12 at room temperature and convert with decreasing width to simpler domain patterns. Details of these complex changes can be found in [108–112] and earlier references cited therein.

Another class of materials, multiferroics, which are both ferroelectric and antiferromagnetic, has attracted considerable attention recently because of their potential applications in multifunctional devices. $BiFeO_3$ is particularly attractive because of its high ferroelectric polarization, its high ferroelectric Curie temperature and high antiferromagnetic Néel temperature and has, therefore, been studied recently by XMLD-PEEM, combined with piezoelectric force microscopy [113]. The study revealed a clear correlation between the ferroelectric and the antiferromagnetic domains and antiferromagnetic domain switching induced by ferroelectric domain switching could be observed. Other fundamental studies of antiferromagnetic materials were concerned with the spin structure of antiferromagnetic surfaces (NiO) and thin layers. These will be discussed in section 4.3 in connection with ferromagnetic–antiferromagnetic interfaces.

XMCD-PEEM studies of ferromagnetic layers also brought some new fundamental insight. One of them concerns the spin reorientation transition from perpendicular to in-plane magnetization and back to perpendicular magnetization with increasing thickness in a 1–3 ML thick Fe wedge on a Ni layer on Cu(100) [114]. The study found a reduction of the Curie temperature within a narrow region of the spin reorientation transition. Another study was concerned with a quite different fundamental problem, 'superferromagnetism', a phenomenon occurring in discontinuous films consisting of single domain ferromagnetic nanoparticles. In another study, multilayer films of $Co_{80}Fe_{20}$ nanoparticles separated by 3 nm thick Al_2O_3 layers showed an extreme magnetic softness and extremely rough domain walls [115].

4.2. Magnetic domain structure in small ferromagnetic patterns

Small ferromagnetic patterns play an important role in magnetic data storage. While in practical applications only the remanent (0, 1) states and the switching behaviour between 0 and 1 states are of interest, the ability of micromagnetic calculations to predict domain configurations of fabricated patterns needs to be tested. This was the motivation for XMCD-PEEM studies of a large variety of small ferromagnetic Co and Permalloy elements, either produced by electron beam lithography from continuous films [116–118] or growth of three-dimensional crystals [119]. Figure 14 illustrates some of the domain configurations observed in 20 nm-thick rectangular Co patterns with different aspect ratios. For comparison, figure 15 shows micromagnetic simulations for the same thickness and aspect ratios of 1:1 and 1:3 [116]. All configurations correspond to local energy minima of the total energy consisting of stray field energy and exchange energy, which should be reflected in their relative frequency seen in the virgin state of the patterns.

The comparison between experiment and simulation shown in figure 16 confirms that, with some exceptions, this is indeed the case for aspect ratios 1:2 and 1:3. In square patterns the energy of the vortex state is much lower than that of all other states so that it is observed nearly exclusively. Only rarely is the double Landau state seen. The S state is observed only in 10 nm thick films [118]. At the other aspect ratios there is good agreement with a few notable exceptions: the 200 nm wide patterns at aspect ratio 1:2, the svav (cross-tie) and avov (diamond) patterns, occur much more frequently than expected from their energies and at aspect ratio 1:3 the frequency of several patterns does not agree well with the corresponding energies. The first discrepancy may be ascribed to roughness of the edges of the patterns, which is most critical in the narrowest patterns and not taken into account in the simulations, the second one is probably due to the smaller statistics in the larger

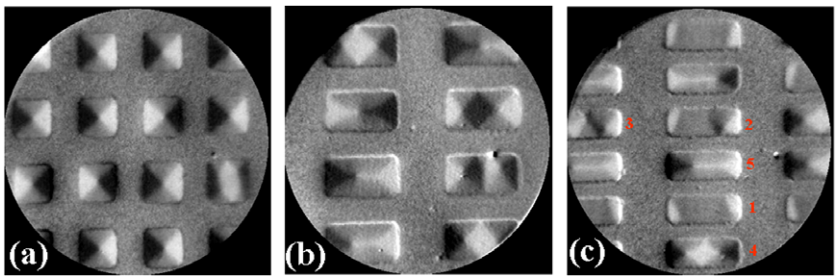

Figure 14. XMCD-PEEM images of rectangular Co patterns with aspect ratios of: (a) 1:1, (b) 1:2 and (c) 1:3. The photon beam is from the left. Field of view 5 μm. Reproduced from [116]. Copyright 2005 with permission from the American Institute of Physics.

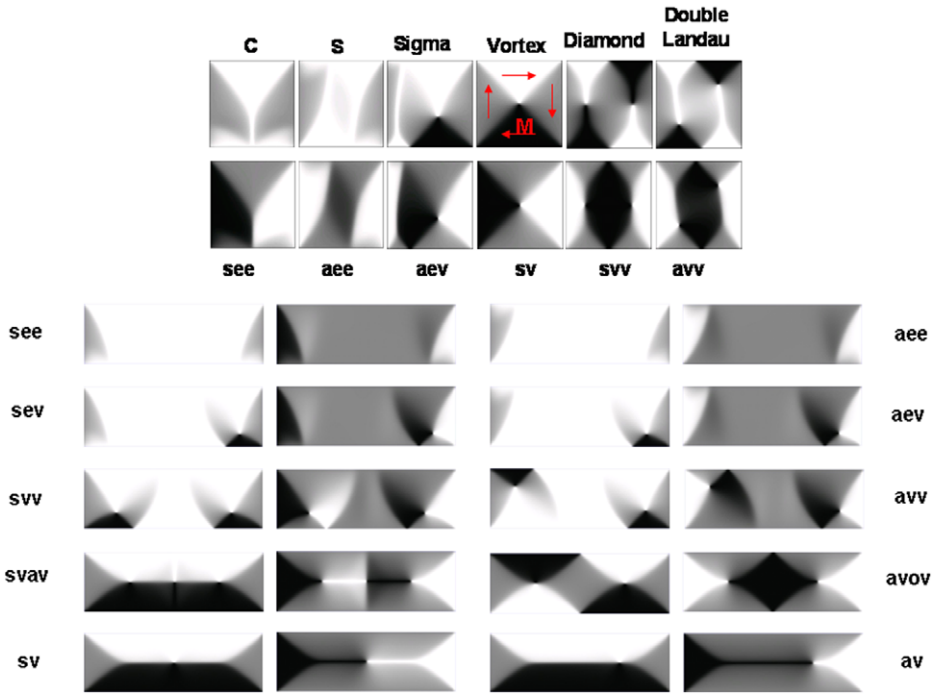

Figure 15. Micromagnetic simulations of the magnetization distribution with minimum local total energy for 20 nm thick Co elements. Width 200–600 nm. The grey levels correspond to the XMCD contrast for horizontal and vertical illumination in the figure. The symbols refer to the kind of domains formed. Symbols on first place a, s: for asymmetric, symmetric. Subsequent symbols a, e, o, v: for antivortex, edge, no vortex, vortex (colour online). Reproduced from [116]. Copyright 2005 with permission from the American Institute of Physics.

patterns. Another factor that limits the comparability between simulation and experiment is the thickness accuracy. This is limited by measurement accuracy during growth and possibly by thickness change during sputtering which has been used to reduce the thickness of the protective layer in order to enhance the magnetic contrast.

Some of these limitations are eliminated in the study of epitaxial three-dimensional crystals grown on single crystal surfaces at elevated temperatures. In this case the dimensions and shape of the crystals can be measured with a high degree of accuracy by a variety of methods such as STM or LEEM and can be reproduced in the simulations. Figure 17 [119] shows an example of a Co crystal on a Mo(110) surface. As in the case of the MnAs domains discussed before, the magnetization distribution in the near-surface region agrees very well (within the resolution limit of the image) with the micromagnetic simulations, which also give the magnetization distribution within the crystal. Figure 17 is a good example of the power of SPELEEM: it allows accurate *in situ* measurements of the crystals with LEEM and LEED, the latter allowing determination of the facet orientation.

Another group of patterns that has been studied considerably in recent years are rings [117, 118, 120–125] and slotted rings [118], the latter because of their low switching field range [126]. Figure 18 gives an overview of the domain structures of these patterns in the remanent state. Complete rings can have no domain walls in the so-called vortex state (a), or two domain walls in the so-called onion state, either vortex walls (b) or transverse walls as shown here for slotted rings ((c), (d)). Whether the vortex state or vortex walls or transverse walls form depends upon thickness and width of the rings. At large ring widths and thickness vortex walls form, at small widths and thickness transverse walls form [117, 122]. In 10 nm thick films, the thinnest studied, complex magnetization

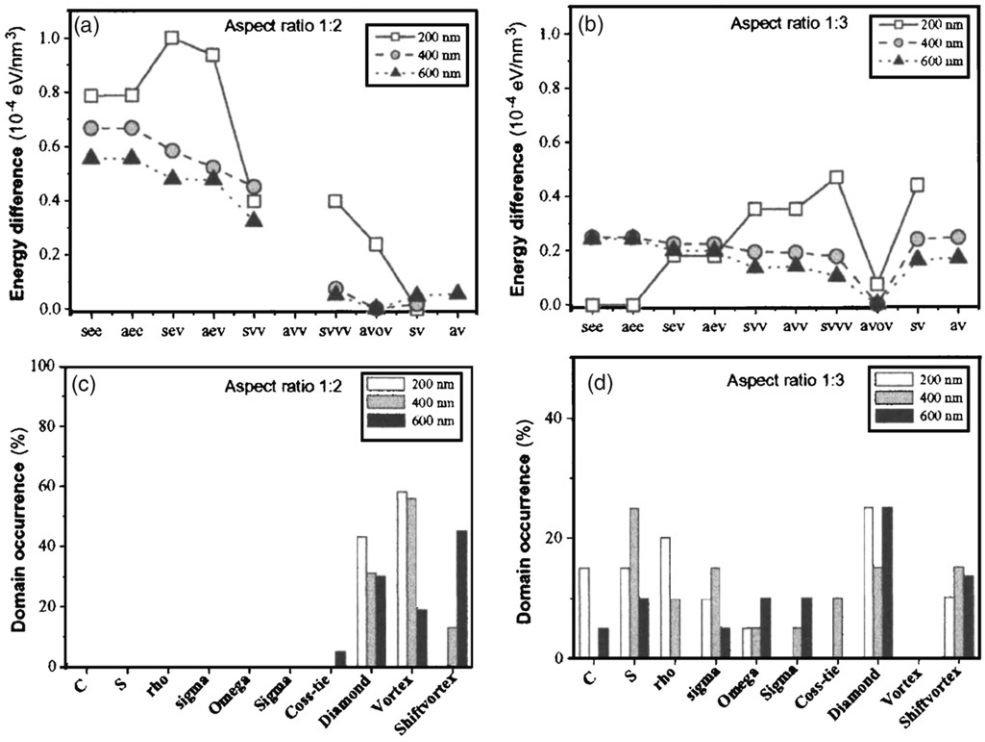

Figure 16. Comparison between simulation and experiment. (a), (b) Energy differences between the various configurations and the configuration with minimum energy; (c), (d) frequency with which the various configurations have been observed. (a), (c) Aspect ratio 1:2; (b), (d) aspect ratio 1:3. Reproduced from [116]. Copyright 2005 with permission from the American Institute of Physics.

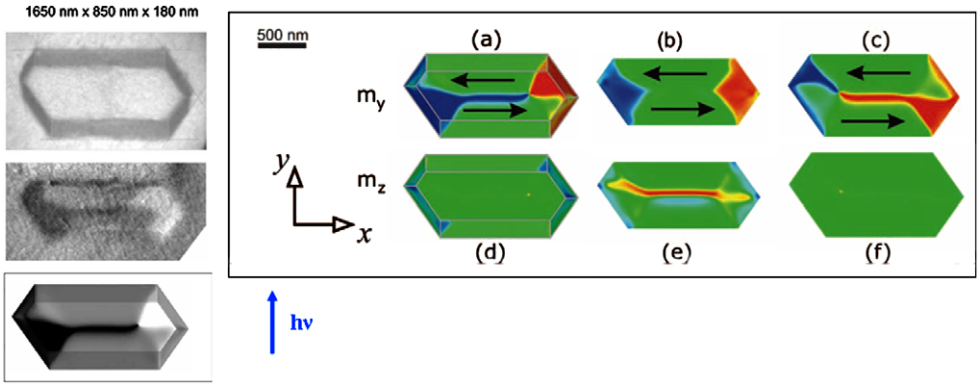

Figure 17. Domain structure of a 180 nm thick three-dimensional Co crystal on a Mo(110) surface. Left side from top to bottom: LEEM image, XMXD-PEEM image, micromagnetic simulation of magnetization in the top region of the crystal. Right side: simulation of (a)–(c) y-component, (d)–(f) z-component of the magnetization, (a), (d) top, (b), (e) centre, (c), (f) bottom of crystal (colour online). Reproduced from [123] with copyright permission.

patterns appear at large widths [117], some of which have been explained by micromagnetic simulations [125]. The complexity of the domain structure is attributed to the lower stray field energy and to the stronger influence of defects in the thinnest films.

The magnetization distribution in the slotted rings in the virgin state is frequently more complicated than shown in figure 18; in the remanent state it depends strongly upon the width and size of the rings, the slot angle and obviously upon the orientation of the slot with respect to the applied field. Figure 19 shows some examples for a slot angle of 90°. In (a) the walls have moved to the open ends and appear to be vortex walls, in (b) the vortex state appears with comparable frequency as the state with the transverse wall. When the slot is oriented in the same direction as the applied field (b), only the vortex state remains with equal probability of clockwise and counter-clockwise magnetization with decreasing size and width. In (c) and (d) a comparison of virgin and remanent states is shown for rings with slot orientation perpendicular to the applied field. In orientation (a) several configurations are present in the virgin state (c), while in the remanent state (d) many patterns have switched in the direction of the

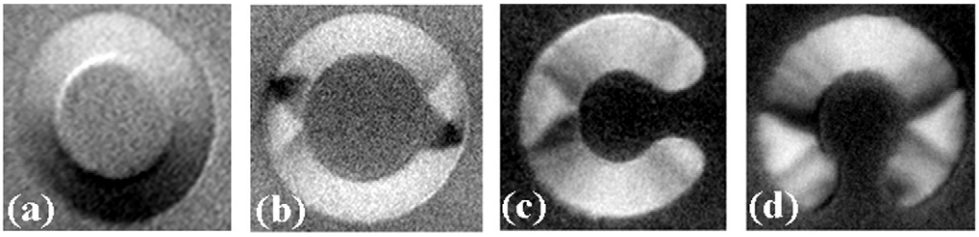

Figure 18. Magnetization distribution in the remanent state of complete and slotted Co rings: (a), (b) with 2400 nm outer diameter and 350 nm width and (b), (c) with 1600 nm outer diameter and 400 nm width. (a) Vortex configuration; (b) onion state with two vortex walls; (c), (d) one and two transverse walls, respectively. The applied field and plane of incidence of the light in the XMCD-PEEM images are in the horizontal direction. Reproduced from [118] with permission. Copyright 2006 John Wiley & Sons Limited.

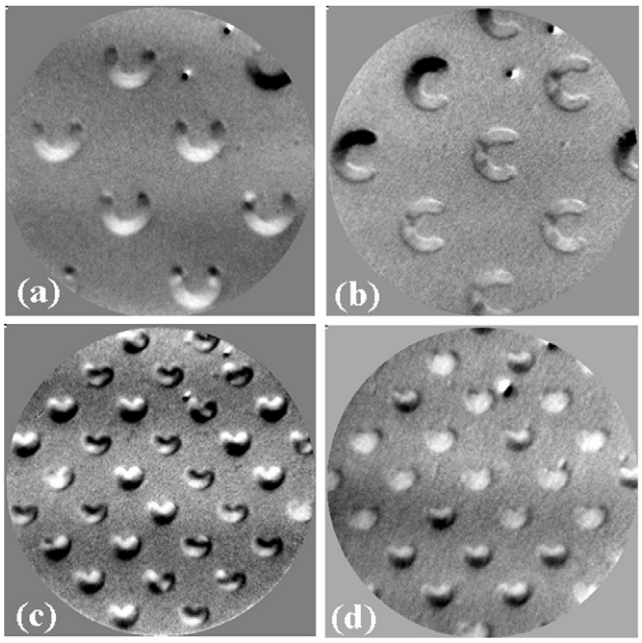

Figure 19. XMCD-PEEM images of slotted Co rings. (a), (b) Comparison of two slot orientations with respect to the applied field (remanent state, outer diameter 800 nm, width 150 nm). (c), (d) Comparison of virgin and remanent state (outer diameter 400 nm, width 175 nm). Field and light direction (horizontal) as in figure 18.

applied field. Figures 19(c) and (d) illustrate the present limits of XMCD-PEEM in identifying complex domain structures. Another study close to the limits of the magnetic resolution of this method was concerned with 500 nm wide $La_{0.7}Sr_{0.3}MnO_3$ patterns which show domain structures similar to those shown above [127].

In ferromagnetic/nonmagnetic/ferromagnetic trilayers the domain structure can be more complicated because top and bottom layers have their own domain structure, which are, however, magnetically coupled. The remanent states of Permalloy/Cu/Permalloy trilayer discs with 1.2–2.5 μm diameter have been studied and compared with micromagnetic simulations [128, 129].

Finally it should be mentioned that self-organized ferromagnetic stripes on vicinal refractory surfaces have also been studied and correlated with their structure [130]. Concluding this section, XMCD-PEEM studies have not only given considerable insight in the magnetization distribution in small patterns but also shown that micromagnetic simulations allow a reliable prediction of the magnetization distribution in small well-defined ferromagnetic patterns. This is true for the single-crystalline example discussed. In polycrystalline patterns prepared by lithographic methods defects and edge roughness can cause differences between simulation and experiment, but with this limitation in mind, the agreement is good as shown by the first example. XMCD-PEEM, however, sees only the near-surface region so that thicker samples require micromagnetic simulations for complete characterization of the magnetization distribution.

4.3. Ferromagnetic–antiferromagnetic interfaces

Ferromagnetic–antiferromagnetic interfaces play a fundamental role in computer and data storage technology where they are used to pin the magnetization of the hard layer in a fixed direction during the switching of the soft layer in spin valves and magnetic tunnel junctions. The mechanism of this pinning, which causes a shift of the hysteresis curve, the so-called exchange bias, has been the subject of XMCD-PEEM and XMLD-PEEM studies for nearly 10 years using several model systems: Co/NiO, Co/$LaFeO_3$, Co/FeMn and Ni/FeMn. Work prior to 2004 has been well reviewed [7, 8] so that here only the more recent work will be discussed briefly.

Early work, discussed in these previous reviews, had focused on interface reactions that form at the annealing temperatures used during cooling in an applied field, for example at Co/NiO interfaces. In the reaction, the uncompensated spins are formed, which are believed to be responsible for the exchange bias. The interface wall energy and the interface exchange stiffness of the Co/NiO(100) interface were determined more recently by XMLD/XMCD-PEEM measurements [131]. Other work has concentrated on interface roughness, grain size [132] and orientation [133]. Also strain plays a mayor role in XMLD effects and can dominate the XMLD signal as demonstrated by polarization-dependent x-ray absorption spectroscopy [134, 135]. Another interesting observation is the anisotropy axis rotation transition of epitaxial NiO films on Fe(100), in which the axis rotates from perpendicular to in-plane orientation between 1.5 and 2.5 nm thickness [136].

Figure 20 shows an example of studies of $LaFeO_3$ epitaxial layers with Co as a ferromagnetic overlayer [132].

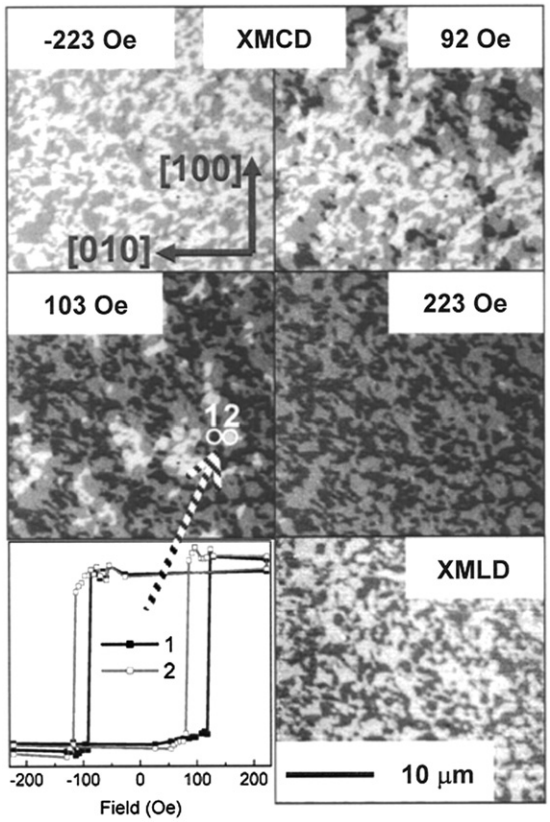

Figure 20. Switching of Co domains exchange-coupled to an epitaxial $LaFeO_3$ layer. Magnetic field and light direction along [100]. The upper four Co XMCD-PEEM images show the magnetization distribution at various field strengths during a field sweep. The hysteresis curve is obtained form the grey levels of black and white domains. The magnetization of grey domains is perpendicular to the applied field. The Fe XMLD image at the bottom shows the size of the antiferromagnetic domains in the $FeLaO_3$ layer. Reproduced from [132]. Copyright 2004 with permission from the American Institute of Physics.

The (001)-oriented film consists of many small domains with four different orientations of the out-of-plane ⟨110⟩ antiferromagnetic axes whose projections onto the surface plane are parallel to the [100] and [010] directions. The interface coupling magnetizes the Co in the corresponding directions. Application of a field in the [100] direction switches the Co domains magnetized in the ±[100] direction (black and white regions) but not those with magnetization perpendicular to the field (grey regions). Measurements of the grey level in individual domains after applying field pulses with increasing magnitude gave the hysteresis curves 1 and 2 with opposite exchange bias field corresponding to the two antiferromagnetic axes in this projection. In a statistical analysis the bias field was found to increase linearly with decreasing domain diameter as expected for a random distribution of pinned, uncompensated spins. In another study [137] it was noted that annealing in oxygen increases the domain size and order of $LaFeO_3$ films.

Other ferromagnetic/antiferromagnetic layer systems studied extensively in connection with exchange pinning are Co and Ni on FeMn [138–142]. The aim was the understanding of the spin structure of FeMn using the interlayer coupling-determined magnetization direction in the ferromagnetic layer as an indicator. In part their aim was also at a deeper understanding of the exchange coupling. By using crossed wedges of the individual layers and nonmagnetic interlayers between them a wealth of information was obtained, too extensive to do justice to in this brief review. Reference [141] gives a good account of some of this work. In the bilayer system Fe/MnPd on MgO(100) the influence of the exchange bias direction on the domain structure of the Fe layer after magnetization in different directions was clearly demonstrated by XMCD-PEEM [143]. Finally one study was concerned with the influence of ion bombardment on the magnetization patterns of MnIr/CoFe nanostructures [144].

4.4. Magnetization dynamics

The understanding of the switching process of magnetic elements in computers is of fundamental importance for improving their speed, which has stimulated efforts to understand the dynamics of switching. Studies in this direction may be grouped in two classes: stroboscopic pump–probe experiments and 'before–after' experiments. The former require complete reversibility, the latter complete irreversibility after each probe pulse. The experimental techniques used in pump–probe experiments have been described in section 2.7, those used in before–after studies will be briefly mentioned in connection with their results.

Several pump–probe studies have been devoted to the understanding of the response of different parts (vortex, domains with magnetization antiparallel and perpendicular to the applied field) of small patterns to magnetic field pulses [18–20, 145–147]. Depending upon pulse length and repetition frequency the vortex may rotate [18] or move linearly [19] or reverse direction when short bursts of an AC field are applied [148]. Figure 21 shows an example of how domains with magnetization antiparallel to the field respond to the pulse [20, 145]. During the fast rise of the field a ripple develops in these regions of rectangular Permalloy patterns due to local incoherent rotation of the magnetization perpendicular to the field. During the decay of the field, it acts effectively in the opposite direction, causing the ripple to spread into the domain with magnetization parallel to the applied field and to split the vortex. The edge roughness seen is an effect of the stray field of the ripple structure, which deflects the slow secondary electrons used for imaging. In the domains with magnetization perpendicular to the field, the field exerts a torque on the magnetization, which tilts it away from its equilibrium state. This causes a precession of the magnetization, which relaxes back into its equilibrium state via damped precessions as illustrated in figure 22 [19]. From these data the frequencies and decay time of two oscillators were extracted. Whilst the precession eigenmodes have frequency in the GHz mode, the domain walls move at lower speed (270 MHz). The vortex moves perpendicular to the excitation field and relaxes without showing the rotating motion observed in the earlier experiments mentioned above [18]. More recently these studies were extended to the more complex svav domain structure of figure 15 which led to the understanding of the

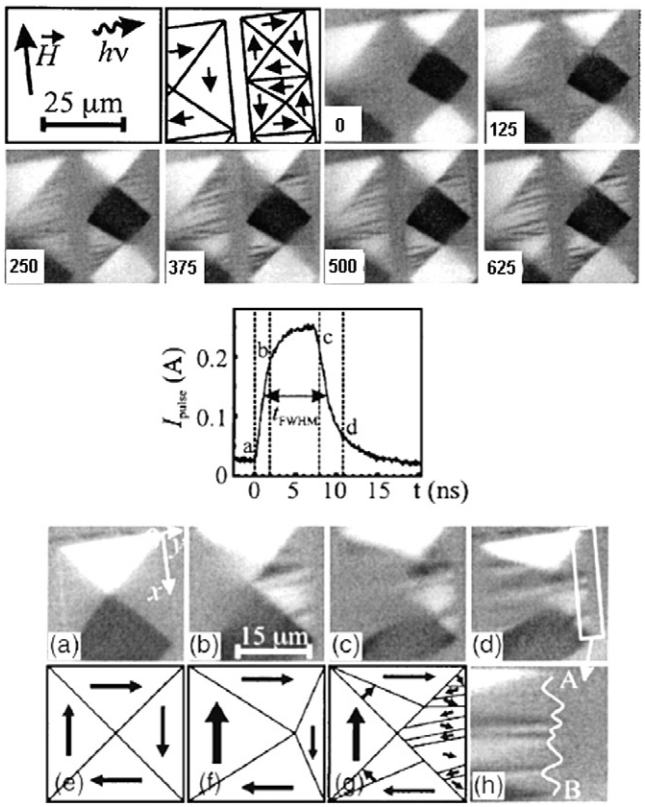

Figure 21. Stroboscopic pump–probe XMCD-PEEM images of the change of the magnetization distribution in 40 nm thick, 20×80 μm^2 Permalloy patterns during application of the magnetic field pulse shown. The numbers are in ps after the onset (a) of the pulse. The directions of the applied field and of the photon beam are shown in the upper left. The magnetization distribution is schematically indicated in the lower part. Each image is accumulated from about 10^7 pulses. Reproduced from [145]. Copyright 2004 with permission from the American Institute of Physics.

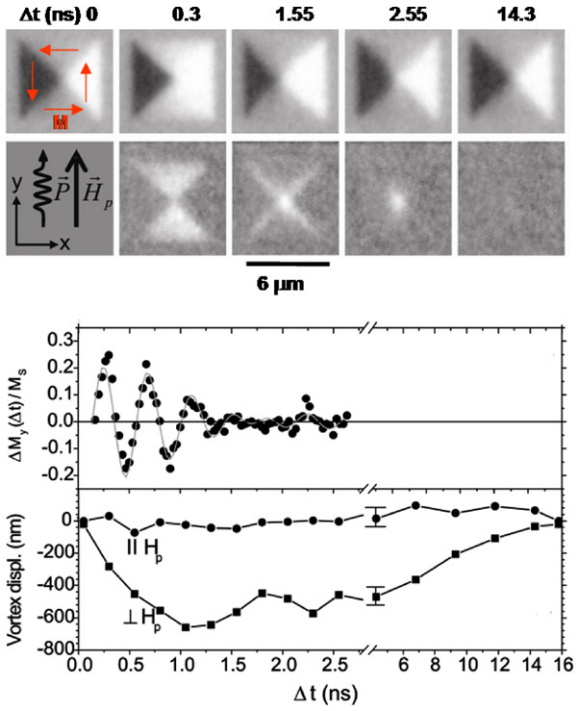

Figure 22. Top: Stroboscopic pump–probe XMCD-PEEM images of the change in the magnetization distribution in 30 nm thick, 6×6 μm^2 Permalloy patterns upon applying a 450 ps field pulse H_p of 60 Oe along the y direction. The lower images are difference images between the corresponding upper images and the image taken at $\Delta t = 0$. Bottom: the upper curve shows the M_y component in the domains with $\mathbf{M} \perp \mathbf{H}_p$, the lower curve the displacement of the vortex. No significant change is seen in the domains in which $\mathbf{M} \parallel \mathbf{H}_p$. Each image is accumulated from 3×10^{-8} pulses (colour online). Reprinted with permission from [19]. Copyright 2005 by the American Physical Society.

dynamics of vortex–antivortex interactions [149]. AC field pump–probe experiments of the av domain structure of figure 15 showed that the initial symmetric domain structure could not only be driven into an asymmetric state but even into a single domain state magnetized perpendicular to the applied AC field [150].

Stroboscopic measurements have also been used to study the switching of the soft layer in spin valves [151] and tunnel junctions [152, 153] by field pulses, using Permalloy/Cu/Co and Permalloy/Al_2O_3/Co trilayers. Domain wall length and domain wall stray field were found to have a significant effect on the speed and mode of propagation of the domain walls. The same types of spin valves and tunnel junctions were also the subject of before–after experiments, again with the goal of understanding the influence of the domain walls and of the coupling on the switching process [154, 155]. Both unipolar and bipolar pulses with increasing field strength were used and the parameters that determine the domain wall propagation were obtained. At high sweep rates the magnetization reversal was found not to occur by domain wall propagation but by nucleation, independent of the interface roughness-induced coupling [154].

While all these experiments studied magnetization processes induced by an applied field, a recent experiment looked at current-induced processes [156]. In this experiment the propagation and spin structure of vortex walls was studied as a function of current density of 11 μs pulses. Figure 23 shows on top the geometry of the experiment and below some of the results. The 28 nm thick and 100 nm wide Permalloy stripes form a zigzag structure. Shape anisotropy and an applied field produce the opposite magnetization indicated by white arrows in neighbouring segments. At the intersection a vortex wall forms. The current induces not only a domain wall motion in the current direction but also multiplication and annihilation of domain walls as illustrated in the lower part of the figure. The propagation speed of the walls was found to depend strongly upon the type of wall. Single vortices have a much higher speed than walls that transform, while multiple vortices were essentially immobile. The results were found to be in good agreement with theory of the spin torque effect that predicts a force on the vortex core.

5. Outlook and perspectives

The combination of PEEM with the newly developed free electron laser sources might relatively soon open up

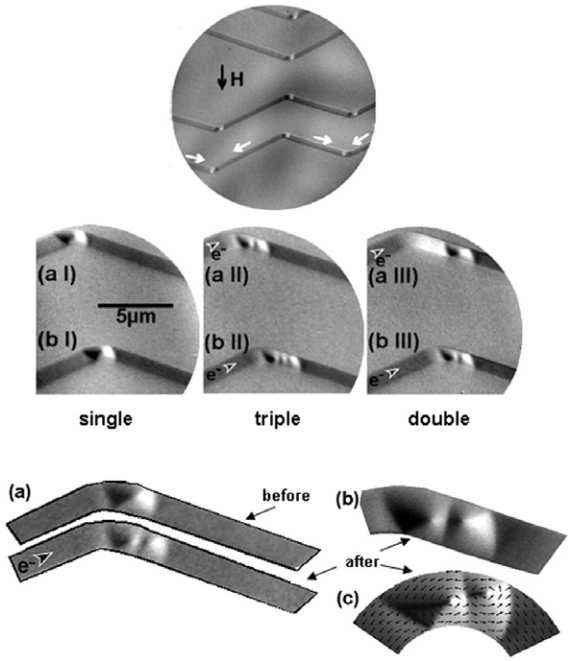

Figure 23. XMCD-PEEM images taken before and after applying a current pulse to 28 nm thick and 100–2000 nm wide Permalloy zigzag structures. For explanation see text. Reproduced from [156] with copyright permission.

unexplored possibilities. In principle, FELs will allow the study of electronic excitations in nanostructures and the photon–surface interaction. These experiments will be based on the pump–probe methods already developed for time resolved UV-PEEM, a technique which has been used to study the dynamics of collective charge oscillations (e.g. surface plasmons) and their unique dissipative properties [157–163]. It is still too early to predict whether the currently developed soft x-ray free electron laser (XFEL) sources can be successfully employed to perform photoelectron spectro-microscopy. The limited repetition rate and tunability of XFELs could make experiments time-consuming and even impractical. Furthermore, their high peak power (in the range of GW) points to severe space-charge problems, which might affect both lateral and energy resolution in PEEM instruments. Such effects have already been observed in UV-PEEM imaging excited by frequency-doubled Ti laser light [164]. On the other hand, space-charge did not hamper recent near-threshold UV-FEL-PEEM experiments at high lateral resolution [104, 105] at average power of few tens of mW using photon energies in the range 3–6.3 eV [103].

We believe, however, that the most significant benefits will come from aberration-corrected (AC) instruments, once the mirror correctors are available and the microscope mechanical and electronic stabilities improved. The better lateral resolution combined with high transmission will allow imaging of structures with lateral size well below 30 nm, approaching problems that are currently not accessible. In this regard, the study of nanoparticles with properties determined by quantum effects could become an important application field. The novel generation of instruments will be able to study clusters of only few nanometres diameter. For example, the aberration-corrected SMART instrument is expected to reach a limiting lateral resolution of less than 1 nm for a photoelectron kinetic energy higher than 20 eV and energy spread of 1 eV [25, 165]. This is sufficient to image the small Au particles on the $TiO_2(110)$ surface discussed in section 3.2 using Au 4f electrons, following the evolution of their cluster morphology and reactivity with varying reaction conditions. Another application where gain in transmission and resolution is of particular importance may be the characterization of nanotubes functionalized by catalyst adatoms or clusters.

The much higher transmission in the corrected instruments mentioned above, compared to the currently best uncorrected instruments, allows a correspondingly smaller photon dose for equivalent image acquisition, which is essential for samples particularly sensitive to beam damage such as oxides, organics and biological materials. We remark the photon-induced damage is the main issue for the above systems, so that an increase in the collection efficiency will allow minimization of the irradiation dose, and thus its effects. Due to the very low duty cycle of stroboscopic experiments, dynamic magnetic imaging will also benefit both from the gain in transmission and resolution offered by AC instruments. Magnetic switching processes in thin film elements discussed in section 4 give an obvious application example.

In conclusion, there is little doubt that aberration-corrected instruments will broaden the application fields of synchrotron-based PEEM tremendously and will lead to much deeper and more detailed understanding of many surface and thin film phenomena. Indeed, with such developments on the horizon, the future of XPEEM looks very exciting.

References

[1] Günther S, Kaulich B, Gregoratti L and Kiskinova M 2002 *Prog. Surf. Sci.* **70** 187
[2] Bauer E and Schmidt T 2003 Multi-method high resolution surface analysis with slow electrons *High Resolution Imaging and Spectroscopy of Materials* ed F Ernst and M Ruehle (Berlin: Springer) p 363
[3] Bauer E 2001 *J. Electron Spectrosc. Relat. Phenom.* **114–116** 976
[4] Bauer E 2001 *J. Phys.: Condens. Matter* **13** 11391
[5] Fecher G H, Hwu Y and Swiech W 1997 *Surf. Sci.* **377–379** 1106
[6] Stöhr J, Padmore H A, Anders S, Stammler T and Scheinfein M R 1998 *Surf. Rev. Lett.* **5** 1297
[7] Feng J and Scholl A 2007 Photoemission microscopy *Science of Microscopy* ed P W Hawkes and J C H Spence (Berlin: Springer) pp 657–95
[8] Stöhr J and Siegmann H C 2006 *Magnetism,* Part III (Berlin: Springer) pp 313–476
[9] De Stasio G, Gilbert B, Frazer B H, Nealson K H, Conrad P G, Livi V, Labrenz M and Banfield J F 2001 *J. Electron. Spectrosc. Relat. Phenom.* **114–116** 997
[10] De Stasio G *et al* 2006 *Clin. Cancer Res.* **12** 206
[11] Chan C S, De Stasio G, Welch S A, Girasole M, Frazer B H, Nesterova M V, Fakra S and Banfield J F 2004 *Science* **303** 1656
[12] Anders S, Padmore H A, Duarte R M, Renner T, Stammler T, Scholl A, Scheinfein M, Stöhr J, Seve L and Sinkovic B 1999 *Rev. Sci. Instrum.* **70** 3973
[13] Bauer E, Koziol C, Lilienkamp G and Schmidt Th 1997 *J. Electron Spectrosc. Relat. Phenom.* **84** 201

[14] Schmidt Th, Heun S, Slesak J, Diaz J, Prince K C, Lilienkamp G and Bauer E 1998 *Surf. Rev. Lett.* **5** 1287
[15] Locatelli A, Abelle L, Mentes T O, Kiskinova M and Bauer E 2006 *Surf. Interface Anal.* **38** 1554–7
[16] Fink R *et al* 1997 *J. Electron Spectrosc. Relat. Phenom.* **84** 1249
[17] Feng J *et al* 2005 *J. Phys.: Condens. Matter* **17** S1339
[18] Choe S-B, Acremann Y, Scholl A, Bauer A, Doran A, Stöhr J and Padmore H A 2004 *Science* **304** 420
[19] Raabe J, Quitmann C, Back C H, Nolting F, Johnson S and Buehler C 2005 *Phys. Rev. Lett.* **94** 217204
[20] Schneider C M, Krasyuk A, Nepijko S A, Oelsner A and Schönhense A 2006 *J. Magn. Magn. Mater.* **304** 6
[21] Tonner B P and Harp G R 1989 *J. Vac. Sci. Technol.* A **7** 1
[22] Harp G R, Han Z L and Tonner B P 1990 *J. Vac. Sci. Technol.* A **9** 2566
[23] Aballe L, Barinov A, Locatelli A, Heun S and Kiskinova M 2004 *Phys. Rev. Lett.* **93** 196103
[24] Wichtendahl R *et al* 1998 *Surf. Rev. Lett.* **5** 1249
[25] Schmidt Th *et al* 2002 *Surf. Rev. Lett.* **9** 223
[26] Wan W, Feng J, Padmore H A and Robin D S 2004 *Nucl. Instrum. Methods Phys. Res.* A **519** 222
[27] Wan W, Feng J and Padmore H A 2006 *Nucl. Instrum. Methods Phys. Res.* A **564** 537
[28] Tonner B P and Harp G R 1988 *Rev. Sci. Instrum.* **59** 853
[29] Swiech W, Fecher G H, Ziethen Ch, Schmidt O, Schönhense G, Grzelakowski K, Schneider C M, Frömter R and Kirschner J 1997 *J. Electron Spectrosc. Relat. Phenom.* **84** 171
[30] Kleineberg U, Menke D, Hamelmann F, Heinzmann U, Schmidt O, Fecher G H and Schönhense G 1999 *J. Electron Spectrosc. Relat. Phenom.* **103** 931
[31] Frazer B H, Girasole M, Wiesed L M, Franz T and De Stasio G 2004 *Ultramicroscopy* **99** 87
[32] Renault O, Barrett N, Bailly A, Zagonel L F, Mariolle D, Cezar J C, Brookes N B, Winkler K, Kromker B and Funnemann D 2007 *Surf. Sci.* **601** 4727
[33] Chmelik J, Veneklasen L and Marx G 1989 *Optik* **83** 155
[34] Cruise D R 1964 *J. Appl. Phys.* **35** 3080
[35] Bauer E 1991 *Ultramicroscopy* **36** 52
[36] Schönhense G and Spiecker H 2002 *J. Vac. Sci. Technol.* B **20** 2526
[37] Oelsner A, Krasyuk A, Fecher G H, Schneider C M and Schönhense G 2004 *J. Electron Spectrosc. Relat. Phenom.* **137–140** 757
[38] Koshikawa T, Shimizu H, Amakawa R, Ikuta T, Yasue T and Bauer E 2005 *J. Phys.: Condens. Matter* **17** S1371
[39] Chao W, Harteneck B, Liddle J A, Anderson E and Attwood D 2005 *Nature* **435** 1210
[40] Gregoratti L 2007 private communication
[41] Gregoratti L *et al* 2004 *Rev. Sci. Instrum.* **75** 4
[42] Günther S, Kolmakov A, Kovac J and Kiskinova M 1998 *Ultramicroscopy* **75** 35
[43] Cocco D, Marsi M, Kiskinova M, Prince K C, Schmidt T, Heun S and Bauer E 1999 *Proc. SPIE* **3767** 271
[44] Quitmann C, Flechsig U, Patthey L, Schmidt T, Ingold G, Howells M, Janousch M and Abela R 2001 *Surf. Sci.* **480** 173
[45] Sasaki S 1994 *Nucl. Instrum. Methods Phys. Res.* A **347** 87
[46] Quitmann C and Nolting F 2007 private communication
[47] Bianco A, Sostero G and Cocco D 2002 *Proc. SPIE* **4782** 74
[48] Moreno T, Belkhou R, Cauchon G and Idir M 2005 *Proc. SPIE* **5921** 0F1
[49] Thole B T, Carra P, Sette F and Van der Laan G 1992 *Phys. Rev. Lett.* **68** 1943
[50] Carra P, Thole B T, Altarelli M and Wang X 1993 *Phys. Rev. Lett.* **70** 694
[51] Carra P and Altarelli M 1990 *Phys. Rev. Lett.* **64** 1286
[52] Roth Ch, Hillebrecht F U, Rose H and Kisker E 1993 *Phys. Rev. Lett.* **70** 3479
[53] Schönhense G 2004 *J. Electron Spectrosc. Relat. Phenom.* **137–140** 769
[54] Neeb D, Krasyuk A, Oelsner A, Nepijko S A, Elmers H J, Kuksov A, Schneider C M and Schönhense G 2005 *J. Phys.: Condens. Matter* **17** S1381
[55] Bonfim M, Ghiringhelli G, Montaigne F, Pizzini S, Brookes N B, Petroff F, Vogel J, Camarero J and Fontaine A 2001 *Phys. Rev. Lett.* **86** 3646
[56] Oelsner A, Schmidt O, Schicketanz M, Klais M, Schönhense G, Mergel V, Jagutzki O and Schmidt-Böcking H 2001 *Rev. Sci. Instrum.* **72** 3968
[57] Schiller F, Heber M, Servedio V D P and Laubschat C 2004 *Phys. Rev.* B **70** 125106
[58] Aballe L, Barinov A, Locatelli A, Mentes T O and Kiskinova M 2007 *Phys. Rev.* B **75** 115411
[59] Hellman A 2005 *Phys. Rev.* B **72** 201403(R)
[60] Binggeli N and Altarelli M 2006 *Phys. Rev. Lett.* **96** 036805
[61] Feibelman F J 1983 *Phys. Rev.* B **21** 1993
[62] Ratto F, Rosei F, Locatelli A, Cherifi S, Fontana S, Heun S, Szkutnik P D, Sgarlata A, De Crescenzi M and Motta N 2004 *Appl. Phys. Lett.* **84** 4526
[63] Ratto F, Locatelli A, Fontana S, Kharrazi S, Ashtaputre S, Kulkarni S K, Heun S and Rosei F 2006 *Small* **2** 401
[64] Ratto F, Rosei F, Locatelli A, Cherifi S, Fontana S, Heun S, Szkutnik P D, Sgarlata A, De Crescenzi M and Motta N 2005 *J. Appl. Phys.* **97** 043516
[65] Schmidt Th, Flege J I, Gangopadhyay S, Clausen T, Locatelli A, Heun S and Falta J 2007 *Phys. Rev. Lett.* **98** 066104
[66] Robinson J T, Liddle J A, Minor A, Radmilovic V, Yi D O, Greaney P A, Long N Y, Chrzan D C and Dubon O D 2005 *Nano Lett.* **5** 2070
[67] Robinson J T, Ratto F, Moutanabbir O, Heun S, Locatelli A, Mentes T O, Aballe L and Dubon O D 2007 *Nano Lett.* **7** 2655
[68] Locatelli A, Pabisiak T, Pavlovska A, Mentes T O, Aballe L, Kiejna A and Bauer E 2007 *J. Phys.: Condens. Matter* **19** 082202
[69] Mentes T O, Locatelli A, Aballe L, Pavlovska A, Bauer E, Pabisiak T and Kiejna A 2007 *Phys. Rev.* B **76** 155413
[70] Ercolani D, Lazzarino M, Mori G, Ressel B, Sorba L, Locatelli A, Cherifi S, Ballestrazzi A and Heun S 2005 *Adv. Funct. Mater.* **15** 587
[71] Mori G, Lazzarino M, Ercolani D, Sorba L, Heun S and Locatelli A 2005 *J. Appl. Phys.* **97** 114324
[72] Mori G, Lazzarino M, Ercolani D, Biasiol G, Sorba L, Heun S and Locatelli A 2005 *J. Appl. Phys.* **98** 114303
[73] Mori G, Lazzarino M, Ercolani D, Biasiol G, Locatelli A, Sorba L and Heun S 2006 *Nucl. Instrum. Methods* B **246** 39
[74] Lazzarino M, Mori G, Sorba L, Ercolani D, Biasiol G, Heun S and Locatelli A 2006 *Surf. Sci.* **600** 3739
[75] Imbihl R and Ertl G 1995 *Chem. Rev.* **95** 697 and references therein
[76] Schaak A, Günther S, Esch F, Schütz E, Hinz M, Marsi M, Kiskinova M and Imbihl R 1999 *Phys. Rev. Lett.* **83** 1882
[77] De Decker Y, Marbach H, Hinz M, Günther S, Kiskinova M, Mikhailov A S and Imbihl R 2004 *Phys. Rev. Lett.* **92** 198305
[78] Locatelli A, Heun S and Kiskinova M 2004 *Surf. Sci.* **566–568** 1130
[79] Locatelli A, Sbraccia C, Heun S, Baroni S and Kiskinova M 2005 *J. Am. Chem. Soc.* **127** 2351
[80] Locatelli A, Mentes T O, Aballe L, Mikhailov A S and Kiskinova M 2006 *J. Phys. Chem.* B **110** 19108
[81] Locatelli A, Aballe L, Mentes T O, Guo F Z and Kiskinova M 2006 *Surf. Sci.* **601** 4663
[82] Locatelli A and Kiskinova M 2006 *Chemistry* **12** 8890–6
[83] Hildebrand M, Mikhailov A S and Ertl G 1998 *Phys. Rev.* E **58** 5483

[84] Hildebrand M, Mikhailov A S and Ertl G 1998 *Phys. Rev. Lett.* **81** 2602
[85] De Decker Y and Mikhailov A S 2004 *J. Phys. Chem.* B **108** 14759
[86] Prabhakaran K *et al* 2003 *Langmuir* **19** 10629
[87] Biasiol G, Heun S, Golinelli G B, Locatelli A, Mentes T O, Guo F Z, Hofer C, Teichert C and Sorba L 2005 *Appl. Phys. Lett.* **87** 223106
[88] Morin C *et al* 2001 *J. Electron Spectrosc. Relat. Phenom.* **121** 203
[89] Morin C, Hitchcock A P, Cornelius R M, Brash J L, Urquhart S G, Scholl A and Doran A 2004 *J. Electron Spectrosc. Relat. Phenom.* **137–140** 785
[90] Hitchcock A P, Morin C, Zhang X, Araki T, Dynes J, Stöver H, Brash J, Lawrence J R and Leppard G G 2005 *J. Electron Spectrosc. Relat. Phenom.* **144–147** 259
[91] Zharnikov M, Shaporenko A, Paul A, Gölzhäuser A and Scholl A 2005 *J. Phys. Chem.* B **109** 5169
[92] Kolmakov A, Lanke U, Karam R, Shin J, Jesse S and Kalinin S V 2006 *Nanotechnology* **17** 4041
[93] Suzuki S, Watanabe Y, Homma Y, Fukuba S-Y, Heun S and Locatelli A 2004 *Appl. Phys. Lett.* **85** 127
[94] Suzuki S, Watanabe Y, Homma Y, Fukuba S-Y, Locatelli A and Heun S 2005 *J. Electron Spectrosc. Relat. Phenom.* **144–147** 357
[95] Griffith O H and Rempfer G F 1985 *Annu. Rev. Biophys. Biophys. Chem.* **14** 113
[96] Labrenz M *et al* 2000 *Science* **290** 1744
[97] Metzler R A, Abrecht M, Olabisi R M, Ariosa D, Johnson C J, Frazer B H, Coppersmith S N and Gilbert P U P A 2007 *Phys. Rev. Lett.* **98** 268102
[98] Gilbert P U P A, Frazer B H and Abrecht M 2005 The organic-mineral interface in biominerals. *Reviews in Mineralogy and Geochemistry Molecular Geomicrobiology* vol 59, ed J F Banfield, K H Nealson and J Cervini-Silva (Washington DC: Mineralogical Society of America) pp 157–85
[99] De Stasio G *et al* 2001 *Cancer Res.* **61** 4272
[100] Gilbert B, Andres R, Perfetti P, Margaritondo G, Rempfer G and De Stasio G 2000 *Ultramicroscopy* **83** 129
[101] Smith A D, Schofield P F, Cresssey G, Cressey B A and Read P D 2004 *Mineral. Mag.* **68** 859
[102] Ade H, English S, Hartman J, Davis R F, Nemanich R J, Litvinenko V N, Pinayev I V, Wu Y and Madey J M J 1998 *Surf. Rev. Lett.* **5** 1257
[103] Edwards G S, Allen S J, Haglund R F, Nemanich R J, Redlich B, Simon J D and Yang W-C 2005 *Photochem. Photobiol.* **81** 711
[104] Yang W-C, Zeman M, Ade H and Nemanich R J 2003 *Phys. Rev. Lett.* **90** 136102
[105] Yang W-C, Ade H and Nemanich R J 2004 *Phys. Rev.* B **69** 045421
[106] Somokhvalov A, Garguilo J, Yang W-C, Edwards G S, Nemanich R J and Simon J D 2004 *J. Phys. Chem.* B **108** 16334
[107] Ye T, Hong L, Garguilo J, Pawlak A, Edwards G S, Nemanich R J, Sarna T and Simon J D 2006 *Photochem. Photobiol.* **82** 733
[108] Däweritz L *et al* 2005 *J. Vac. Sci. Technol.* B **23** 1759
[109] Zdyb R, Locatelli A, Heun S, Cherifi S, Belkhou R and Bauer E 2005 *Surf. Interface Anal.* **37** 239
[110] Engel-Herbert R *et al* 2006 *Appl. Phys.* A **84** 231
[111] Engel-Herbert R *et al* 2006 *J. Magn. Magn. Mater.* **305** 457
[112] Däweritz L, Kolovos-Vellianitis D, Trampert A, Herrmann C, Ploog K H, Bauer E, Locatelli A, Cherifi S and Heun S 2006 *J. Physique* IV **132** 159
[113] Zhao T *et al* 2006 *Nat. Mater.* **5** 823
[114] Won C *et al* 2005 *Phys. Rev.* B **71** 224429
[115] Bedanta S, Eimüller T, Kleemann W, Rhensius J, Stromberg F, Amaladass E, Caradoso S and Freitas P P 2007 *Phys. Rev. Lett.* **98** 176601
[116] Cherifi S, Hertel R, Kirschner J, Wang H, Belkhou R, Locatelli A, Heun S, Pavlovska A and Bauer E 2005 *J. Appl. Phys.* **98** 043901
[117] Zdyb R, Pavlovska A, Locatelli A, Heun S, Cherifi S, Belkhou R and Bauer E 2005 *Appl. Surf. Sci.* **249** 38
[118] Bauer E, Belkhou R, Cherifi S, Hertel R, Heun S, Locatelli A, Pavlovska A, Zdyb R, Agarwal N and Wang H 2006 *Surf. Interface Anal.* **38** 1622
[119] Hertel R, Fruchart O, Cherifi S, Jubert P-O, Heun S, Locatelli A and Kirschner J 2005 *Phys. Rev.* B **72** 214409
[120] Kläui M *et al* 2004 *J. Magn. Magn. Mater.* **272–276** 1631
[121] Kläui M *et al* 2004 *Physica* B **343** 343
[122] Kläui M, Vaz C A F, Bland J A C, Heyderman L J, Nolting F, Pavlovska A, Bauer E, Cherifi S, Heun S and Locatelli A 2004 *Appl. Phys. Lett.* **85** 5637
[123] Laufenberg M *et al* 2006 *Appl. Phys. Lett.* **88** 052507
[124] Laufenberg M *et al* 2006 *Appl. Phys. Lett.* **88** 212510
[125] Kläui M, Rüdiger U, Vaz C A F, Bland J A C, Cherifi S, Locatelli A, Heun S, Pavlovska A, Bauer E and Heyderman L J 2006 *J. Appl. Phys.* **99** 08G308
[126] Hu H, Wang H, McCartney M R and Smith D J 2006 *Phys. Rev.* B **73** 153401
[127] Takamura Y, Chopdekar R V, Scholl A, Doran A, Liddle J A, Harteneck B and Suzuki Y 2006 *Nano Lett.* **6** 1287
[128] Buchanan K S, Guslienko K Yu, Choe S-B, Doran A, Scholl A, Bader S D and Novosad V 2005 *J. Appl. Phys.* **97** 10H503
[129] Buchanan K S, Guslienko K Yu, Doran A, Scholl A, Bader S D and Novosad V 2005 *Phys. Rev.* B **72** 134415
[130] Fruchart O, Eleoui M, Vogel J, Jubert P O, Locatelli A and Ballestrazzi A 2004 *Appl. Phys. Lett.* **84** 1335
[131] Scholl A, Liberati M, Arenholz E, Ohldag H and Stöhr J 2004 *Phys. Rev. Lett.* **92** 247201
[132] Scholl A, Nolting F, Seo J W, Ohldag H, Stöhr J, Raoux S, Locquet J-P and Fompeyrine J 2004 *Appl. Phys. Lett.* **85** 4085
[133] Czekaj S, Nolting F, Heyderman L J, Willmott P R and van der Laan G 2006 *Phys. Rev.* B **73** 020401
[134] Haverkort M, Csiszar S I, Hu Z, Altieri S, Tanaka A, Hsieh H H, Lin H-J, Chen C T, Hibma T and Tjeng L H 2004 *Phys. Rev.* B **69** 020408
[135] Cziszar S I, Haverkort M W, Hu Z, Tanaka A, Hsieh H H, Lin H-J, Chen C T, Hibma T and Tjeng L H 2005 *Phys. Rev. Lett.* **95** 187205
[136] Finazzi M, Brambilla A, Biagoni P, Graf J, Gweon G-H, Scholl A, Lanzara A and Duò L 2006 *Phys. Rev. Lett.* **97** 097202
[137] Grepstad J K, Takamura Y, Scholl A, Hole I, Suzuki Y and Tybell Th 2005 *Thin Solid Films* **486** 108
[138] Kuch W, Chelaru L I, Offi F, Wang J, Kotsugi M and Kirschner J 2004 *Phys. Rev. Lett.* **92** 017201
[139] Wang J, Kuch W, Chelaru L I, Offi F, Kotsugi M and Kirschner J 2004 *J. Phys.: Condens. Matter* **16** 9181
[140] Wang J, Kuch W, Chelaru L I, Offi F and Kotsugi M 2005 *Appl. Phys. Lett.* **86** 122504
[141] Kuch W, Chelaru L I, Offi F, Wang J, Kotsugi M and Kirschner J 2006 *Nat. Mater.* **5** 128
[142] Won C, Wu Y Z, Zhao H W, Scholl A, Doran A, Kim W, Owens T L, Jin X F and Qiu Z Q 2005 *Phys. Rev.* B **71** 024406
[143] Blomqvist P, Krishnan M and Ohldag H 2005 *Phys. Rev. Lett.* **94** 107203
[144] Höink V, Sacher M D, Schmalhorst J, Reiss G, Engel D, Weis T and Ehresmann A 2006 *Phys. Rev.* B **73** 224428
[145] Schneider C M *et al* 2004 *Appl. Phys. Lett.* **85** 2562
[146] Krasyuk A, Wegelin F, Nepijko S A, Elmers H J and Schönhense G 2005 *Phys. Rev. Lett.* **95** 207201
[147] Buess M, Raabe J, Perzlmaier K, Back C H and Quitmann C 2006 *Phys. Rev.* B **74** 100404

[148] Van Waeyenberge B *et al* 2006 *Nature* **444** 461
[149] Kuepper K, Buess M, Raabe J, Quitmann C and Fassbender J 2007 *Phys. Rev. Lett.* **99** 167202
[150] Wegelin F, Krasyuk A, Elmers H-J, Nepijko S A, Schneider D M and Schönhense G 2007 *Surf. Sci.* **601** 4694
[151] Kuch W, Vogel J, Camarero J, Fukumoto K, Pennec Y, Pizzini S, Bonfim M and Kirschner J 2004 *Appl. Phys. Lett.* **85** 440
[152] Vogel J *et al* 2005 *Phys. Rev.* B **72** 220402
[153] Fukumoto K, Kuch W, Vogel J, Romanens F, Pizzini S, Camarero J, Bonfim M and Kirschner J 2006 *Phys. Rev. Lett.* **96** 097204
[154] Pennec Y *et al* 2004 *Phys. Rev.* B **69** 180402
[155] Fukumoto K, Kuch W, Vogel J, Camarero J, Pizzini S, Offi F, Pennec Y, Bonfim M, Fontaine A and Kirschner J 2005 *J. Magn. Magn. Mater.* **293** 863
[156] Kläui M *et al* 2006 *Appl. Phys. Lett.* **88** 232507
[157] Gloskovskii A *et al* 2006 *Appl. Phys. Lett.* **100** 084330
[158] Cinchetti M, Oelsner A, Fecher G H, Elmers H J and Schönhense G 2003 *Appl. Phys. Lett.* **83** 1503
[159] Cinchetti M and Schönhense G 2005 *J. Phys.: Condens. Matter* **17** S1319
[160] Cinchetti M, Gloskovskii A, Nepjiko S A, Schönhense G, Rochholz H and Kreiter M 2005 *Phys. Rev. Lett.* **95** 047601
[161] Kubo A, Onda K, Petek H, Sun Z, Jung Y S and Kim H K 2005 *Nano Lett.* **5** 1123
[162] Chelaru L I, Horn-von Hoegen M, Thien D and Meyer zu Heringdorf F-J 2006 *Phys. Rev.* B **73** 115416
[163] Meyer zu Heringdorf F-Z, Chelaru L I, Möllenbeck S, Thien D and Horn-von Hoegen M 2007 *Surf. Sci.* **601** 4600
[164] Lilienkamp G 2007 private communication
[165] Preikszas D 1995 *PhD Thesis* TU Darmstadt